Pontificia Universidad Católica del Perú

Escuela de Posgrado

Tesis

Chemomechanical study of silicon composite anodes for lithium-ion batteries

Para obtener el grado de:
Magíster en Ingeniería y Ciencia de los Materiales

Presentado por: Christopher Alcides Rojas Dávalos

Tutor Responsable (TU Ilmenau): Dr. Michael Stich
Professor Responsable (TU Ilmenau): Prof. Dr. rer. nat. habil. Dr. h.c. Andreas Bund

Professor Responsable (PUCP): MSc. Magali Karina Camargo León

Fecha y Lugar: 14/10/2021, Lima

Declaration of originality

I hereby declare that this thesis was created autonomously without using other than the stated references. All parts which are cited directly or indirectly are marked as such. This thesis has not been used in the same or similar forms in parts or total in other examinations.

14th October 2021, Ilmenau

Christopher Alcides Rojas Dávalos

Acknowledgments

This work represents the end of a stage in my life that would not have come to a successful conclusion if it were not for the support and company of my family, friends, and colleagues.

I am deeply grateful to my advisors, Prof. Andreas Bund, Dr. Michael Stich and MSc. Magali Camargo who supported the development of this thesis and guided my scientific learning during this process. Likewise, my thanks go to Prof. Rolf Grieseler, whose support, contribution, and interest to this thesis were like those of an advisor.

Thanks also to Prof. Andreas Rosenkranz and colleagues from the Ningbo Institute of Materials Technology and Engineering of China who provided the Ti_3C_2 MXene powder, main and critical material for the development of this work.

In addition, my thanks to the members of the Electrochemistry and Electroplating research group, particularly to MSc. Mario Kurniawan and MSc. Gisella Lucero, friends that I met in the group and who supported me with their knowledge, ideas but also with their enjoyable company in the laboratory.

To my family who supported me from the moment I decided to pursue this master's degree and who, despite the distance, have always been attentive to my development and well-being.

Finally, I also would like to thank ProCIENCIA (Programa Nacional de Investigación Científica y Estudios Avanzados) that funded my first stay in Germany with the grant 137-2018-FONDECYT (Proyecto: "Estancia en Cooperación con DAAD Alemania")

Resumen

El sillico (Si) es considerado uno de los candidatos que puede reemplazar al grafito en ánodos de baterías de ion litio debido a su capacidad para almacenar mayor energía y, por ende, de mejorar sus rendimientos. No obstante, el alto estrés mecánico causado por su alta variación volumétrica durante los ciclos de carga y descarga sumado a su baja conductividad eléctrica viene siendo un impedimento para su amplio uso. Por tal motivo, los composites a base de silicio son estudiados en esta tesis con el fin de mejorar su viabilidad comercial.

Este trabajo de investigación se enfoca en la síntesis de composites MXeno Ti_3C_2 - silicio como ánodos para baterías de iones de litio así como su caracterización electroquímica. El MXeno Ti_3C_2 es un material dos dimensional cuya buena resistencia mecánica y conductividad pueden aportar a solucionar los problemas de los ánodos de Si. La caracterización de los materiales de partida (partículas de Si y MXeno Ti_3C_2) consistió en el estudio de su morfología por microscopía electrónica de barrido (SEM), distribución de tamaños por dispersión dinámica de luz (DLS), composición química por espectroscopia de energía dispersiva (EDS) y microestructura por difracción de rayos X (XRD). Distintas composiciones de materiales de electrodo fueron preparados mediante una suspensión aplicada sobre una lámina de cobre por la técnica del recubrimiento con cuchilla y caracterizados mediante microscopia óptica y SEM. Asimismo, se prepararon semiceldas con dichos electrodos para ser sometidos a ciclos de carga y descarga a distintas corrientes. Los procesos electroquímicos fueron estudiados mediante espectroscopia de impedancia electroquímica (EIS).

Los resultados revelaron que la adición de partículas de Ti_3C_2 promueve que los electrodos puedan alcanzar el 80% y 89% de su capacidad teórica cuando el Ti_3C_2 representa el 20% y 40% de la masa del material activo del electrodo, respectivamente, en comparación al 56% alcanzado por el electrodo de Si puro. Esta mejora es explicada por una reducción de la resistencia a la transferencia de carga observada en los resultados de EIS. Finalmente, el electrodo con 20 % en peso de Ti_3C_2 (640 mAh/g) obtuvo la mejor capacidad específica tras 100 ciclos de carga y descarga, por encima de lo obtenido por el electrodo de Si puro (572 mAh/g).

Abstract

Silicon (Si) is considered one of the candidates to replace graphite in lithium-ion battery anodes due to its ability to store more energy and thus improve their performance. However, the high mechanical stress of pure silicon, caused by its high volumetric change during charge and discharge cycles, together with its low electrical conductivity have been an impediment to its wide use. Silicon-based composites are, therefore, studied in this thesis to improve their commercial viability.

This research work focuses on the synthesis of Ti_3C_2 MXene-silicon composites as anodes for lithium-ion batteries and their electrochemical characterization. Ti_3C_2 MXene is a two-dimensional material whose good mechanical strength and conductivity can contribute to solving the problems of Si anodes. The characterization of the starting materials (Si and Ti_3C_2 MXene particles) consisted of the study of their morphology by scanning electron microscopy (SEM), size distribution by dynamic light scattering (DLS), chemical composition by energy dispersive spectroscopy (EDS) and microstructure by X-ray diffraction (XRD). Electrodes of different compositions were prepared using a slurry mixture deposited by blade coating technique onto a copper foil and characterized by optical microscopy and SEM. Also, half cells were prepared with these electrodes and subjected to charge-discharge cycles at different currents. Additionally, the electrochemical processes were studied by electrochemical impedance spectroscopy (EIS).

The results revealed that the addition of Ti_3C_2 promotes that the electrodes can reach 80% and 89% of their theoretical capacity when Ti_3C_2 represents 20% and 40% of active material mass, respectively, compared to 56% achieved by the pure Si electrode. This improvement is explained by a reduction of the charge transfer resistance observed in the EIS results. Finally, the electrode with 80 wt.% Si and 20 wt.% Ti_3C_2 (640 mAh/g) obtained the best specific capacity after 100 charge/discharge cycles, above that obtained by the pure Si electrode (572 mAh/g).

Zusammenfassung

Silizium (Si) gilt als einer der Kandidaten für den Ersatz von Graphit in Anoden von Lithium-Ionen-Batterien, da es mehr Energie speichern und somit die Leistungsfähigkeit verbessern kann. Die hohe mechanische Beanspruchung reinen Siliziums, die durch die starke Volumenänderung während der Lade- und Entladezyklen verursacht wird, sowie seine geringe elektrische Leitfähigkeit haben jedoch bislang eine breite Verwendung verhindert. Daher werden in dieser Arbeit Siliziumkomposite untersucht, um ihre kommerzielle Verwendbarkeit zu verbessern.

Die folgende Studie konzentriert sich auf die Synthese und elektrochemische Untersuchung von Ti_3C_2 MXene-Silizium-Kompositen für Batterieanoden. Ti_3C_2 ist ein zweidimensionales Material, dessen gute mechanische Festigkeit und Leitfähigkeit dazu beitragen kann, die Probleme von Si-Anoden zu lösen. Die Charakterisierung der Ausgangsmaterialien (Si und Ti_3C_2 MXene Partikel) bestand in der Untersuchung ihrer Morphologie durch Rasterelektronenmikroskopie (REM), ihrer Größenverteilung mittels dynamische Lichtstreuung (DLS), ihrer chemischen Zusammensetzung durch energiedispersive Spektroskopie (EDS) und ihrer Kristallstruktur durch Röntgenbeugung (XRD). Elektroden unterschiedlicher Zusammensetzung wurden durch Herstellung einer Elektrodensuspension und anschließendes Rakeln auf eine Kupferfolie aufgebracht und durch optische Mikroskopie und SEM charakterisiert. Außerdem wurden Halbzellen mit diesen Elektroden hergestellt und Lade-Entlade-Zyklen bei verschiedenen Stromstärken durchgeführt. Zusätzlich wurden die elektrochemischen Prozesse durch elektrochemische Impedanzspektroskopie (EIS) untersucht.

Die Ergebnisse zeigen, dass Si durch das Hinzufügen von 20 bis 40% Ti_3C_2 zwischen 80 % und 89 % seiner theoretischen Kapazität erreichen kann. Im Vergleich dazu konnten mit reinem Si nur 56 % der theoretischen Kapazität erreicht werden. Diese Verbesserung erklärt sich durch eine Reduktion des Ladungsübergangswiderstands, die in den EIS-Ergebnissen beobachtet wurde. Die Elektrode mit 80 Gew.% Si und 20 Gew.% Ti_3C_2 erreichte die beste spezifische Kapazität nach 100 Lade-/Entladezyklen (640 mAh/g) gegenüber der der Si-Elektrode (572 mAh/g).

Table of Contents

List of Figures

List of Tables

Symbols and abbreviations

CC	Constant current cycling
CE	Coulombic efficiency
CMC	Carboxymethyl cellulose
CPE	Constant phase element
CV	Constant voltage
CVD	Chemical vapor deposition
DEC	Diethyl carbonate
DFT	Density-functional theory
DI	Deionized
DLS	Dynamic light scattering
DMC	Dimethyl carbonate
DMSO	Dimethyl sulfoxide
EC	Ethylene carbonate
EDS	Electron dispersive X-ray
EIS	Electrochemical impedance spectroscopy
GP	Graphite electrode
GP	Graphite electrode
ICE	Initial coulombic efficiency
LCO	Lithium cobalt oxide
LFP	Lithium iron phosphate
LIB	Lithium-ion battery
LMO	Lithium manganese oxide
LTO	Lithium titanate
MX	MXene electrode
NCA	Lithium nickel cobalt aluminum oxides
NMC	Lithium nickel manganese cobalt oxides
OCV	Open circuit voltage

p-SiNP	Porous silicon nanoparticles
PAA	Poly(acrylic acid)
PAN	Polyacrylonitrile
PDVF	Polyvinylidenefluoride
PE	Polyethylene
PEIS	Potentiostatic electrochemical impedance spectroscopy
PMMA	poly-methyl methacrylate
PP	Polypropelene
PSi	Porous Si nanoparticle
PSN	porous silicon nanospheres
PVDF	Polyvinylidene fluoride
REM	Rasterelektronenmikroskop
RPM	Revolutions per minute
SEI	Solid electrolyte interface
SEM	Scanning electron microscopy
SHE	Standard hydrogen electrode
SiGP40	60% Silicon - 40% graphite composite electrode
SIMX20	80% Silicon - 20% Ti_3C_2 composite electrode
SiMX40	60% Silicon - 40% Ti_3C_2 composite electrode
SiMX80	20% Silicon - 80% Ti_3C_2 composite electrode
SiNP	Silicon nanoparticles
TEM	Transition electron microscopy
TMAOH	tetramethylammonium hydroxide
TMO	transition metal oxides

1 Introduction

1.1 Motivation

The climate concerns caused by human activities have prompted the search for sustainable solutions to mitigate their impact on our environment. Activities like energy consumption and transportation, which in 2018 were responsible of 34% and 14% of the global CO_2 emissions, respectively [1], require alternatives such as renewable energies and electric vehicles to reduce their impact on our climate. However, the forementioned solutions demand a breakthrough in energy storage to be implemented to their full potential. Therefore, in recent years, energy storage systems have been the focus of multiple scientific and engineering developments.

Batteries, in particular lithium-ion batteries (LIB), are a type of electrochemical energy storage with a promising future in meeting these demands. In fact, they are already widely used to store and supply energy in applications such as electric vehicles, power grid systems, smartphones, medical equipment, and many other daily-life electronic devices. As a result, LIBs market is forecast to grow by 75 % from 2020 to 2025 [2], and this demand will only increase as our society moves towards a more electrified economy. To meet the demanding requirements of current and future applications, the research has been focused on developing new materials for LIBs, especially for the components that dictate the capacity of a battery, also called active materials. To date, many options for cathode active materials have been developed such as transition metal oxides containing Co, Ni and Mn [3]; however, carbonaceous materials, such us graphite, remain the primary choice for anodes since the development of the first commercial lithium-ion battery by Sony in 1991 [4]. Therefore, a breakthrough in anode materials is required, as commercial cells reach the maximal theoretical specific capacity of graphite (372 mAh/g).

Silicon (Si) is one of the many candidate materials to replace graphite anodes. It has a theoretical specific capacity (3579 mAh/g) almost ten times higher than graphite and is also available in large quantities in the earth's crust [5]. However, its main problem lies in the high mechanical stress it withstands during cycling (280% volumetric swelling), which generates rapid capacity decay throughout cycles [6]. In

this sense, the mixture of silicon particles with materials that alleviate these stresses by acting as buffers is frequently studied. The most studied material for this purpose is graphite, which has shown to improve capacity retention over many cycles when mixed with Si [7]. In addition, a novel 2D material called Ti_3C_2 MXene has recently shown good cyclability results when mixed with Si [8][9]. MXenes are a family of 2D materials produced from a hexagonal crystal structure precursor material called MAX phase by a selective wet etching process [10]. Due to their particular combination of properties inherited from their MAX-phase precursor such as good mechanical strength and low electrical resistivity, MXenes are expected to be a candidate material for producing Si composite anodes. The few studies conducted on Ti_3C_2 - silicon composites have mainly focused on anode preparation techniques to enhance their specific capacity by improving the interconnection between the two materials, however, no studies have addressed in detail the stress relief mechanism generated by the addition of Ti_3C_2 to silicon-based anodes.

Based on the above, the following work will focus on understanding the role of Ti_3C_2 content on the electrochemical performance of Ti_3C_2 - silicon composite anodes, particularly at long-term cycling. The performance of graphite-silicon anodes will also be studied as a reference to compare the results of the former.

1.2 Research goals

The purpose of this research includes:

- The characterization of the properties of Ti_3C_2 MXene and silicon powders to evaluate their effect on electrode performance. The materials characterization includes the analysis of the morphology, size and the chemical composition of the materials.
- The development of a preparation method to obtain reproducible composite electrodes of Ti_3C_2 – silicon and graphite – silicon by the slurry coating technique.
- The investigation of the electrochemical performance of the prepared electrodes and its relation to the volumetric expansion during cycling.

2. State of the art

2.1 Lithium-ion battery

2.1.1 Lithium-ion battery development

Lithium-ion batteries (LIB), as they are known today, are the result of intensive research that has led to the development of a battery technology with great features and still a high potential for improvement. Their great performance in comparison with other battery technologies relies on the element lithium, which is one of the elements with the most negative electrochemical potential in the periodic table, with a standard potential of -3.04 V against the standard hydrogen electrode (SHE), a low density 0.534 g/cm^3 and theoretically a high gravimetrical capacity of 3860 mAh/g (the calculation consider the mass of deposited Li) [11].

These properties make lithium metal the ideal anode, as confirmed by the first studies conducted in the 1970s which prompted scientific attention to the development of batteries using it as an anode [12]. However, rechargeable lithium metal batteries are still, to these days, an in-development technology due to the problems posed by the formation of lithium dendrites during uneven lithium deposition over several cycles [13]. These dendrites grow until they come into contact with the cathode, leading to short circuits and thermal runaway safety issues.

In order to prevent these problems, carbonaceous materials were seen as a solution to replace lithium metal at the anode due to their ability to electrochemically intercalate lithium at a similar operating voltage (0.1 V vs Li/Li$^+$) and avoid the formation of dendrites [14]. In addition, in the 1980s, research by John B. Goodenough found $LiCoO_2$ to be a prospective cathode material for LIBs due to its high operating voltage (4 V vs. Li/Li$^+$) and decent energy density [15]. With these two components, it was necessary to select an electrolyte capable of remaining stable under high operating voltages to develop a market-ready concept. Therefore, with the already accumulated knowledge of those years, the Japanese company Sony Corporation presented the first-generation commercial lithium-ion battery in 1991 [16]. This battery concept featured an energy density of 200 Wh/dm^3 and 80 Wh/kg

[17] by using $LiCoO_2$, petroleum coke and propylene carbonate as cathode, anode and electrolyte, respectively, and marked the beginning of the huge commercial success of lithium-ion batteries.

2.1.2 Components and operating mechanism

Today's lithium-ion batteries have higher specific energy and use better optimized components compared to Sony's first commercial battery; however, the operating principle remains the same. Its mechanism works on the principles of intercalation and exchange of lithium ions between its electrodes, as exemplified in Figure 2-1 for a $LiCoO_2$ and graphite battery [18]. When a lithium-ion cell is assembled, the Li ions reside at the cathode and thus needs to be charged. By providing energy to the system, electrons flow from the $LiCoO_2$ to the graphite through an external circuit, which promotes the reactions presented in equation 2-1 and 2-2. In particular, the first charging processes of a LIB also include reactions of formation of a solid electrolyte interface (SEI) on the anode surface which prevents further decomposition of the electrolyte in subsequent cycles [19]. Then, when the battery is fully charged and the external circuit is electrically closed, electrons flow from the anode to the cathode spontaneously due to the potential difference between the two, thus producing the reverse reactions.

Anode reaction	$C_6 + xLi^+ + xe^- \rightleftharpoons Li_xC_6$	(2-1)
Cathode reaction	$LiCoO_2 \rightleftharpoons Li_{1-x}CoO_2 + xLi^+ + xe^-$	(2-2)

The materials used to build the battery play an important role in battery performance. In particular, the materials known as active materials are among the components that receive the most scientific attention due to their influence on the total capacity of the battery. These are composed by the materials used in the cathode and anode.

For the former, metal oxides are the usual selection in commercial cells and are usually classified into three groups based on their structure [20]. The first group is composed of transition metal oxides (TMO) of hexagonal layered structure that allocates the transition metal and Li in alternating octahedral interstitial sites. Examples are $LiCoO_2$ (LCO) [21], and variations in which Co is replaced by Ni, Mn

or Al to improve certain properties, such as $LiNi_{0.33}Mn_{0.33}Co_{0.33}O_2$ (NMC) or $LiNi_{0.8}Co_{0.15}Al_{0.05}O_2$ (NCA), which are widely used in electric vehicle application due to their improved energy density [22]. The second group encompasses spinel-structured materials where Li occupies tetrahedral rather than octahedral sites, forming a cubic structure. $LiMn_2O_4$ (LMO) is an example of this group that is preferred in applications where safety is the main priority over high energy density [23]. Finally, the third group consists of polyanion compounds that present an olivine orthorhombic structure where the metal and lithium cations occupy the octahedral sites while the anions form an isolated tetrahedra. The most widely used material in this category is $LiFePO_4$ (LFP), which is often used in power grid systems due to its low cost and high safety [24].

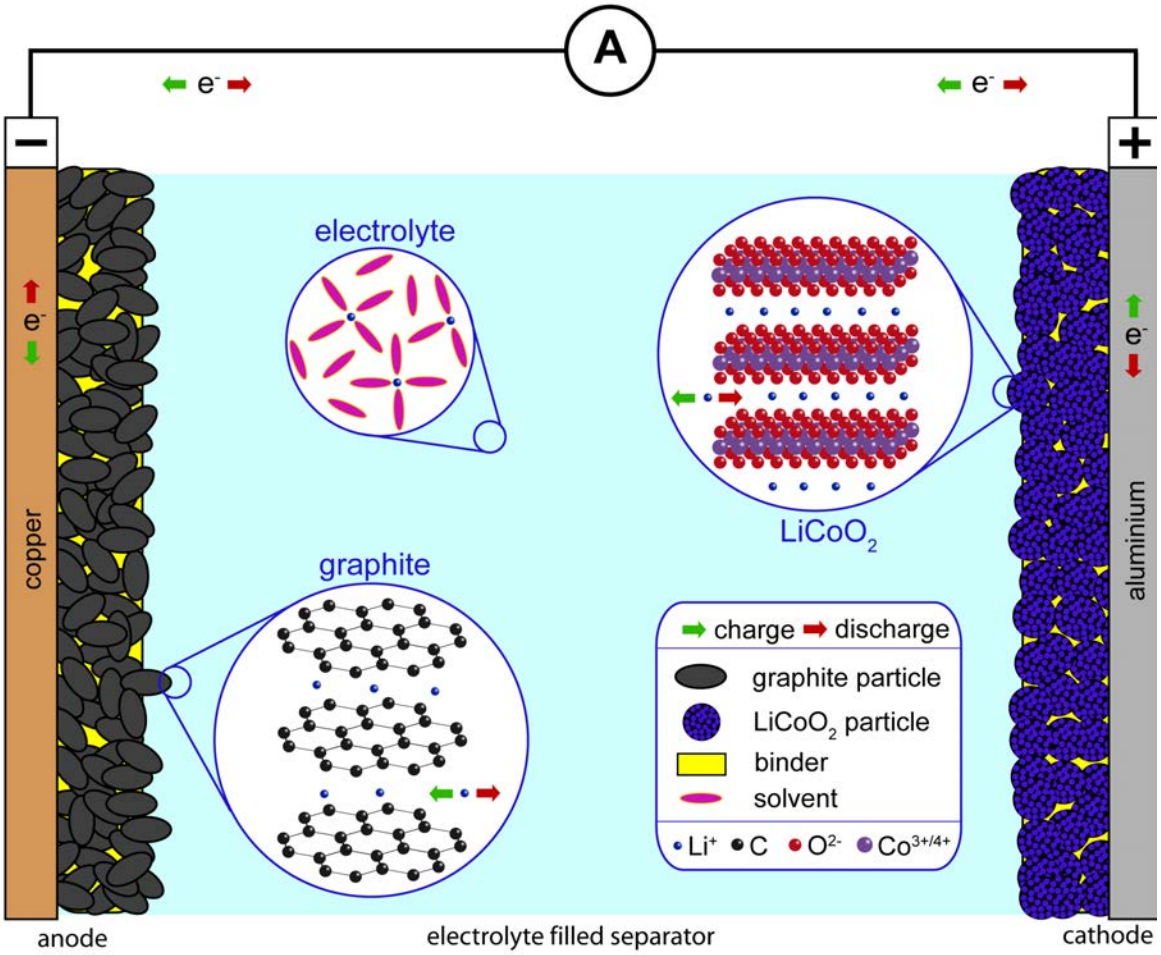

Figure 2-1. Working principle of a lithium-ion conventional cell [25].

On the anode side, carbonaceous materials are preferred due to their low delithiation potential (0.1 V vs. Li/Li^+), good electrical conductivity and diffusivity of lithium ions, low cost and abundance [14]. Of these, graphite is the most widely used due to its high theoretical specific capacity of 372 mAh/g and high initial coulombic efficiency (91%). However, one of the problems faced by graphite is solvent co-intercalation and exfoliation when propylene carbonate is used as the electrolyte [26]. Therefore, disordered graphitic structures are also used to ameliorate this problem. Particularly hard carbons, so named because of the complexity to convert its structure to graphite even at high temperatures, are used due to their higher capacity (460 mAh/g) and their ability to lessen exfoliation. However, their low coulombic efficiency (76 %) makes them less attractive than graphite for current LIBs [27]. Another commercial material used for anodes is lithium titanate oxide (LTO). LTO is a layered structure material that stores lithium ions under intercalation like graphite but with a longer cycle life and safety at fast charging rates [28]. These properties are due to the small expansion it exhibits during lithiation, which is why it is commonly referred to as a "zero stress" material. However, despite its advantages, LTO is less used due to its high price and high operating voltage (1.55 V vs. Li/Li^+). In addition to intercalation anodes, alloy anodes are also often studied because their theoretical specific capacity is several times higher than that of anodes with intercalation storage mechanism [29]. However, these types of materials are not yet fully utilized in commercial batteries due to problems related to the large volumetric expansion they experience during lithiation. Some examples are Sn, Ge and Si. The latter is one of the most promising and is already being used commercially in small quantities in composites with graphite [30]. In the following chapters Si will be discussed in detail.

Among the inactive materials, electrolytes play a crucial role in a battery by transporting lithium ions [31]. Therefore, the electrolyte must meet, in addition to good ionic conductivity, other requirements such as high electrical resistivity and good electrochemical stability. Commercial electrolytes are liquid solutions consisting of three components: a lithium salt, a solvent and additives. The most commonly used lithium salt is $LiFP_6$ due to its good stability (stability window from 1

to 4.7 V vs. Li/Li^+) and its high solubility in carbonate solvents [18]. However, the use of this salt has raised safety concerns due to the formation of HF when in contact with water [32]. Regarding the solvent, the range of possibilities is mainly limited to organic carbonates such as dimethyl carbonate (DMC), due to the high operating voltages of LIBs [33]. In particular, ethylene carbonate (EC) is also used in mixture with the above due to the promotion of stable SEI formation in graphite anodes. Finally, additives are added to the electrolyte to improve certain battery characteristics, such as preventing thermal runaways or the formation of a robust SEI, as in the case of vinylene carbonate [34].

The last components in a battery cell are the separator and current collectors. The former is responsible for preventing short circuits by physically isolating the electrodes but at the same time allowing the transport of lithium ions [35]. Therefore, properties like porosity, porous size, mechanical strength, wettability, and thermal and chemical stability are optimized to meet a balance between the two requirements. Polymeric membranes made of polyolefins like polypropylene (PP) and polyethylene (PE) are most frequently used in commercial batteries and glass fiber membranes are used in laboratory cells when better electrolyte uptake is required. In the case of current collectors, the two principal requirements are that they are good electrical conductors and at the same time chemically stable under oxidation and reduction [36]. Aluminum is the main current collector used in the cathode while copper is used for the anode.

2.2 Silicon anodes

2.2.1 Electrochemical behavior and challenges

The ability of silicon (Si) to react electrochemically with lithium has been extensively studied and it has been confirmed that the $Li_{15}Si_4$ alloy phase is the product of complete lithiation of crystalline Si at room temperature [37], which presents a theoretical capacity of 3579 mAh/g. Although other studies refer that silicon can also form other Si-Li alloy compounds with higher capacities such as $Li_{22}Si_5$ (4200 mAh/g) [38], [39], these phases cannot be produced at ambient conditions and therefore will not be referred in this work as the maximum potential of silicon anodes.

As studied by Obrovac et al. [40], the first lithiation of crystalline Si starts with its conversion into amorphous lithiated Si at a voltage plateau of 170 mV against Li/Li^+. During this plateau, a two-phase structure of amorphous lithiated Si (shell) and a non lithiated crystalline structure (core) coexist. Once the voltage drops below 50 mV, lithiated amorphous Si is transformed into crystalline $Li_{15}Si_4$. On the other hand, the delithiation behavior of Si depends on the voltage reached during the previous lithiation cycle. If Si has been completely transformed to $Li_{15}Si_4$, then a plateau is seen around 450 mV during lithiation, whereas two sloping plateaus are seen if only lithiated amorphous Si is present. In both cases, the delithiation ends with an amorphous Si structure. The following lithiation cycles of the amorphous Si follows the behavior shown in the lithiation curve IV in Figure 2-2.

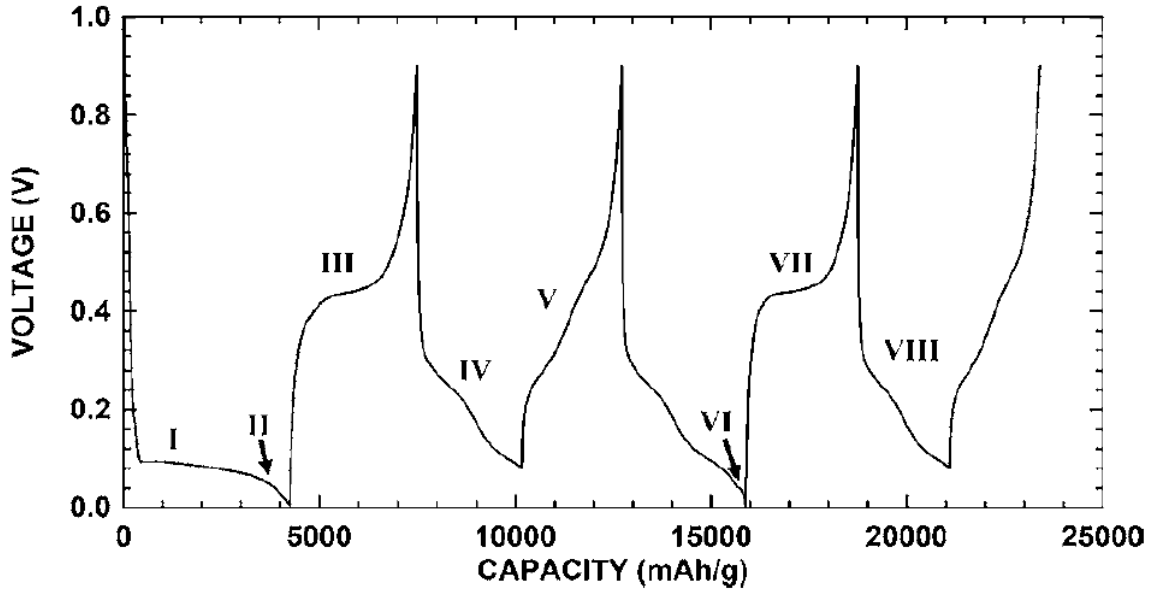

Figure 2-2. Voltage vs. capacity plot of a silicon anode. (I) 170 mV plateau related to the transformation from crystalline Si to lithiated amorphous Si (II, VI) transformation from lithiated amorphous Si to $Li_{15}Si_4$ (III, VII) delithiation of $Li_{15}Si_4$ into amorphous Si (IV, VIII) lithiation of amorphous Si over 170 mV (no phase change) (V) delithiation of partially lithiated amorphous Si [40].

Although silicon anodes present a high theoretical capacity, there are still some challenges and disadvantages that must be overcome to reach their full potential in practical applications. First, Si is a semiconductor material known for its low electrical conductivity (6.7×10^{-4} S/cm). This property affects Si electrodes as they generate higher overpotential losses during cycling compared to commercial graphite anodes

(10^4 S/cm) and, therefore, require often high amounts of conductive agents to reduce the ohmic resistance of the electrodes. Secondly, and by far the most difficult problem of silicon electrodes, are the structural changes during cycling, in particular, the formation of $Li_{15}Si_4$, which is associated with high volumetric expansions and high stresses. This volumetric expansion has been estimated to be 280% based on the density change of $Li_{15}Si_4$ phase [37] and it is associated with anode problems such as deterioration of the electrode structure due the pulverization of the Si particles, loss of electrical contact between the active material and the current collector, and the rapid consumption of the electrolyte due to the continuous reformation of the solid electrolyte interface (SEI) layer [41].

Researchers have focused their attention on developing solutions to overcome these problems and they can be summarized in the following four groups: reduction of Si particle size to nanoscale, variation of the anode morphological structure, preparation of composites with stress-relief buffer matrix (active or inactive materials) and preparation of the slurry with stronger binders [42].

By reducing the particle size, researchers have been able to address the problem of silicon anode fracture. Studies using in situ transmission electron microscopy (TEM) concluded that particles with a diameter greater than 150 nm crack during the first lithiation cycle, while a smaller particle size increases the lifetime of Si anodes [43] and, at the same time, improves the diffusion of lithium ions through their structure. However, the use of nanometer-sized Si particles also presents its own challenges. Nanosized Si anodes typically exhibit large irreversible capacities (initial coulombic efficiency) in the 65-85% range due to their larger surface area and the higher presence of native SiO_2 layer [44]. Si anodes require at least 75% coulombic efficiency (CE) to be comparable to commercial graphite. On the other hand, the mass loading obtained for Si nanoparticle anodes is mostly around 1 mg/cm^2, which is ten times less than what is used for graphite anodes [45]. This metric is equally relevant, since in a Li-ion battery the aim is to maximize the active material content per total weight of the battery.

Adjusting the anode morphology is another common strategy to achieve Si anodes with commercial potential. The synthesis of structures such as silicon nanowires, nanotubes, thin flakes and nanopillars are some examples successfully employed to accommodate silicon volume changes due to its structural anisotropy [46]. Likewise, nanoporous Si structures are another interesting way to adjust Si morphology to accommodate volume expansion due to the presence of void spaces, which also facilitate cycling at high rates due to the enhancement of the diffusion pathway for Li ions [47]. To produce these porous structures, top-down techniques, such as electrochemical and electroless etching, and bottom-up techniques using templates are used. However, it is worth mentioning that, although their performance is better than other types of Si anodes, the structures have high manufacturing costs which limits their application in commercial cells.

The combination of Si with materials that helps to mitigate its expansion has also been proposed. These materials can be classified as active or inactive based on their ability to contribute to the overall electrode capacity [48]. In general, the selected materials focus on the improvement of Si anode cycling performance but at the same time it is desired that they exhibit high electrical conductivity to ameliorate the other Si anode problems discussed above. Examples of inactive materials studied are ceramic compounds such as TiN, TiB_2 and TiC and metals such as Ni, Fe and Cu, while some examples of active materials studied are metals such as Mg and Sn which form compounds with Si like Mg_2Si [42]. Special attention deserves graphite as stress-relief active matrix in Si anodes, which is by far the most studied material for preparing Si composites. Due to its relevance, it will be discussed in more detail in the next chapter of this review.

At last, due to the importance of binders on maintaining a strong adhesion between all the components of Si anodes, intensive research has been done to study suitable binders to restrain Si anode expansion [49]. Synthetic polymer binders such as Polyvinylidenefluoride (PDVF), Poly(acrylic acid) (PAA) and Polyacrylonitrile (PAN) are often used, although expensive organic solvents are required to dissolve them. In contrast, biopolymers such as Carboxymethyl cellulose (CMC) and alginate are

preferable due to their low cost and sustainability and are usually the preferred binders for Si anode production. Finally, conductive polymers such as polyaniline and polypyrrole have also been studied due to their potential to improve electrical conductivity of the Si electrode, however, p-type conductive polymers have shown inferior cycling stability.

2.2.3 Silicon-graphite composite

The use of graphite in combination with Si to produce composite anodes is one of the most studied strategies to enable the commercialization of Si anodes due to its low cost and, above all, its properties to contribute as a relief matrix to mitigate Si expansion. In addition, graphite improves the overall conductivity of the electrode, helps to reduce the first irreversible capacity losses and promotes the formation of a stable SEI layer.

Currently, graphite is the most widely used material in commercial LIB anodes and its electrochemical behavior has been well studied. Graphite is a layered material composed of multiple hexagonally distributed carbon atoms whose lithiation process follows an intercalation mechanism until the formation of LiC_6 phase. This phase is associated with a theoretical maximum specific capacity of 372 mAh/g which is reached when all the available spaces between the graphite layers are occupied. However, different phases occur throughout the lithiation process that can be correlated with defined plateau voltages as shown in Figure 2-3. During the first lithiation, a first plateau is observed around 0.25 V vs Li/Li^+ where a graphite structure with randomly distributed Li ions (Stage 1L) turns into a structure where fully lithiated graphite interlayers spaces are separated by 3 empty ones (Stage 4). As more Li ions are intercalated within the graphite structure, the amount of empty interlayer spaces separating the lithiated ones reduces and two new plateaus are observed at around 0.15 V (Stage 3 to Stage 2) and 0.1 V (Stage 2 to Stage 1) vs Li/Li^+ reaching at the end a LiC_6 structure as was mentioned above. In this last phase, the interlayer space distance must expand 10.4 % to accommodate the intercalation of lithium ions, which represents a large difference compared to what is observed in Si. Finally, during the delithiation process, graphite follows the same structural

changes but in reverse, with the greatest amount of delithiation occurring at plateaus near 0.1 V vs Li/Li$^+$. For this reason, this is commonly referred as the operating voltage of the graphite anodes.

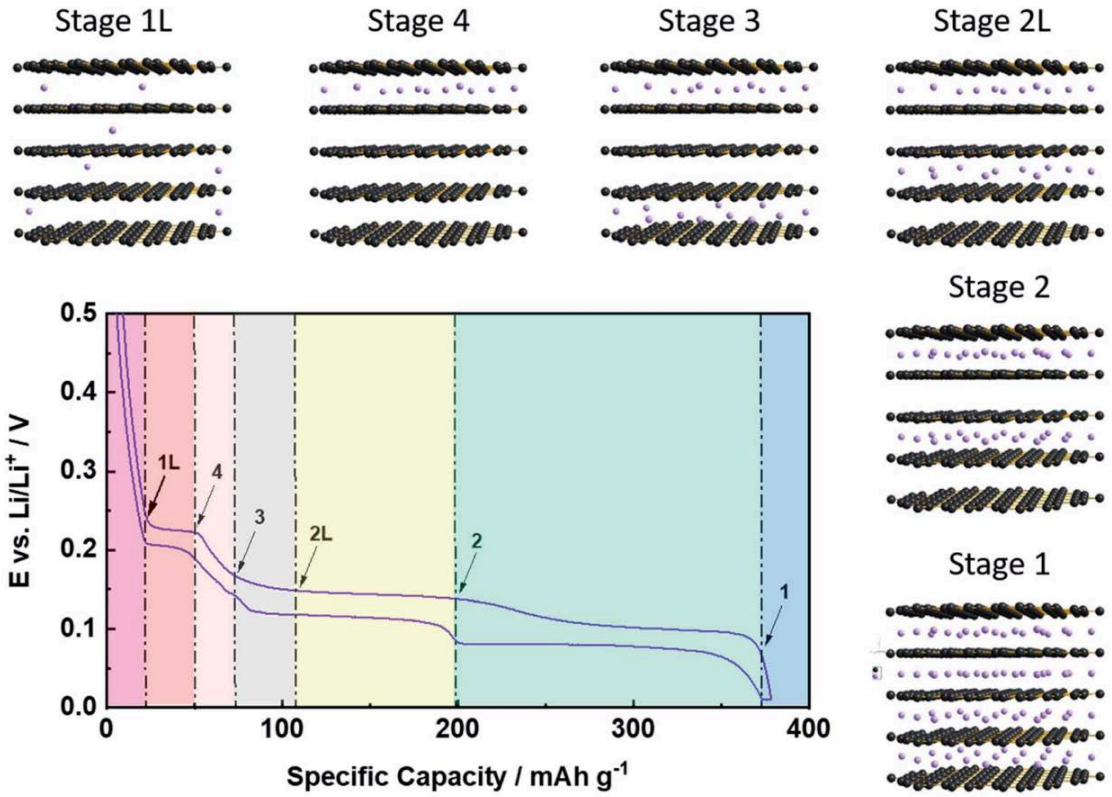

Figure 2-3. Staging mechanism during electrochemical lithiation and delithiation of a graphite anode [4].

Electrochemical galvanostatic cycling of silicon graphite composite anodes follows the same lithiation and delithiation peaks observed for both materials [50]. However, Dose et al. [51] found that, for a 14 % Si wt. silicon graphite composite, three new lithiation peaks were observed at 0.11, 0.17 and 0.2 V vs Li/Li$^+$ with the former contributing with the highest capacity by far of the three. These new peaks were suspected to be related to a charge transfer interaction between silicon and graphite, although no evidence of this was shown. Similar interplay between silicon and graphite was observed by Moon et al. [52] who studied the impact of the interaction between silicon and graphite on anode degradation. They observed crosstalk between surface located Li$^+$ in Si particles to graphite particles during the constant voltage charging and rest steps. Furthermore, they suggested that, aside from the

previously described failure mechanism of Si anodes, the degradation mechanism in silicon-graphite composite anodes is derived from trapped Li ions in the Si particles core and the capacity decay of graphite due to pressure generated by expansion.

To produce Si-graphite anodes, several synthesis methods have been proposed, which directly influence the performance of the composite anodes. Powder blending is one of the simplest and most scalable methods, as the mixture can be processed later with the conventional slurry preparation method used in lithium-ion battery production [53]. This method is usually accompanied by a previous intensive high-energy mechanical milling to homogenize the particle size of both components to achieve better electrochemical performance [54]. This was confirmed by Lee et al. [55] who observed that the greatest improvement in performance of their Ti-Si alloy anode occurred when graphite of similar particle size was added. Another method used to produce Si-graphite anodes is spray drying [56]. This technique involves spraying the dispersion solution through a nozzle, followed by rapid drying using a thermal gas. It has proven to be an effective method for the production of silicon graphite composites due to the performance improvement generated by the formation of internal pores (free spaces for Si expansion) during drying and its scalability. Finally, chemical vapor deposition (CVD) offers the opportunity to synthesize high purity nanoscale Si on a graphite substrate [53]. CVD consists of exposing the graphite substrate to a gaseous precursor (e. g. silane gas, SiH_4) that is decomposed by applying heat or plasma. Tuned structures can be obtained by this method as demonstrated by Kim et al. [57], which deposited Si on holey graphite previously constructed by catalytic hydrogenation. This method produces composites with good adhesion between Si and graphite with a highly controlled thickness, however, with this technique usually mostly thin film anodes have been produced.

2.3. Ti_3C_2 MXene – Silicon composite

2.3.1 Ti_3C_2 MXene: Development, synthesis, and properties

Ti_3C_2 is part of a novel family of 2D materials known as MXenes, which was discovered by Yury Gogotsi and Michael Barsoum's research group at Drexler University while investigating the electrochemical properties of MAX phases as a material for energy storage applications [58]. MAX phases are a group of ternary carbides and nitrides of chemical formula of $M_{n+1}AX_n$ arranged under a hexagonal structure, where M corresponds to a transition metal element, A to an element of group 13 or 14 of the periodic table and X to either C, N or a mixture of both [59]. Due to their unique structure and composition, MAX phases exhibit low electrical resistivity, good mechanical resistance, but also good machinability and a high thermal stability, a combination of properties rarely seen in a single material. In addition, their graphite-like layered structure sparked the interest of Gogotsi and Barsoum to use them as materials for lithium-ion intercalation in battery applications [58]. However, as Nagib's early reports note, the particle size and especially the presence of element A in its structure decrease the lithiation capacity of the Ti_3AlC_2 MAX phase. Therefore, he proposed a method to selectively etch Al from the structure by immersing the Ti_3AlC_2 powder in a 50% hydrofluoric acid (HF) solution for two hours [60]. With this simple and scalable wet etching process, he succeeded in removing the A layer while preserving the hexagonal structure. The resulting new material, Ti_3C_2, was named MXene because of its similarity to graphene. This first discovery opened up a new class of materials of which more than 30 MXenes are known today [61].

The Ti_3C_2 MXene synthesis process has evolved since the first publication in 2011 [60]. However, wet chemical etching is still the main way to produce Ti_3C_2 where HF is the etchant substance mainly used to remove the Al. This method takes advantage of the weaker metallic bond between Ti and Al compared to the stronger covalent bond between Ti and C to react as equations 2-3, 2-4 and 2-5 propose, where solid crystals of AlF_3 are formed. Next, Ti_3C_2 reacts with water or HF due to the charge imbalance on its surface as shown in equation 2-4 and 2-5, respectively. This leads

to the formation of a tunable functionalized Ti_3C_2 multilayer structure which depends on the concentration of the reactants. At this point, Ti_3C_2 layers are weakly attracted to each other by secondary Van der Waals forces, whose spacing can be increased by intercalation of large organic molecules, such as tetramethylammonium hydroxide (TMAOH) or dimethyl sulfoxide (DMSO), to obtain monolayered Ti_3C_2 by sonication [62].

$$Ti_3AlC_2 + 3HF \rightarrow AlF_3 + \frac{3}{2}H_2 + Ti_3C_2 \quad (2\text{-}3)$$

$$Ti_3C_2 + 2H_2O \rightarrow Ti_3C_2(OH)_2 + H_2 \quad (2\text{-}4)$$

$$Ti_3C_2 + 2HF \rightarrow Ti_3C_2F_2 + H_2 \quad (2\text{-}5)$$

To avoid the risk of working directly with a dangerous and corrosive solution such as concentrated HF, alternative methods were developed to produce in-situ HF [63]. These consist of mixing a fluoride salt and hydrochloric acid (HCl) to form HF only during the etching process, thus reducing the possible risk of direct contact with HF. Apart from the improvement in safety, a milder HF etching is produced, which promotes reaction (1-4) over (1-5) and, therefore, Ti_3C_2 is more prone to be functionalized with -O and -OH over -F radicals. In addition, the delamination process is shortened due to the intercalation of salt cations between the layers acting as an expander of the interlayer space and, therefore, Ti_3C_2 produced by this method requires only manual agitation to be delaminated into monolayer structures [64]. Examples of fluoride salts that have shown good results for Ti_3C_2 synthesis are LiF, NaF, KF and NH_4F [65].

Recently, non-fluorinated synthesis routes have also been explored with promising results. For example, Li et al. reported the synthesis of Ti_3C_2 by hydrothermal alkali treatment with NaOH at 270 °C with a yield of 92 wt.% in respect to the Ti_3AlC_2 MAX phase precursors [66]. In addition, Yang et al. proposed an electrochemical corrosion process to obtain Ti_3C_2 in an aqueous electrolyte mixture of NH_4Cl and TMAOH. However, only 40 wt.% yield was obtained with this method [67]. Ti_3C_2 synthesis remains a new and intensive field of research with researchers exploring different mechanisms to obtain MXenes with different surface functional groups.

The properties of Ti_3C_2 MXenes are highly dependent on the functional groups present on its surface [68]. In terms of electrical conductivity, bare Ti_3C_2 is predicted to have similar metallic behavior to its predecessor Ti_3AlC_2; however, the presence of functional groups gives Ti_3C_2 a semiconducting behavior with a tunable bandgap depending on the functional groups [60]. Similarly, the mechanical properties are also affected by the functional groups. According to theoretical calculations, a Young's modulus of 240 GPa is predicted for -F terminated Ti_3C_2 in contrast with the 350 GPa for -O terminated; however, so far no experimental results have been published in this respect [68]. Furthermore, the Ti_3C_2 shows good thermal stability in an inert environment, where decomposition starts to occur at temperatures over 785 °C; however, the stability is severely affected in an oxygen environment, where transformation of its surface into TiO_2 is observed at lower temperatures (250 °C) [69]. Therefore, the stability of Ti_3C_2 in different media should be considered for long-term storage. Habib et al. demonstrated that Ti_3C_2 exhibit rapid oxidation in aqueous media, where almost complete transformation to TiO_2 was observed within 2 weeks [70]. Therefore, it is strongly recommended to store Ti_3C_2 in an inert environment, such as argon, at low temperatures to avoid oxidation.

2.3.2 Ti_3C_2 MXene for energy storage

The use of Ti_3C_2 MXene powder as an active material to build electrodes for energy storage has been one of its most studied applications since its discovery. Early theoretical studies predicted a good ability of Ti_3C_2 to intercalate not only Li but also Na, K and even Ca ions [71]. As for the former, density functional theory (DFT) calculations by Tang et al. [72] showed that bare monolayer Ti_3C_2 can exhibit a theoretical specific capacity of 320 mAh/g, a higher result than its -F and -OH functionalized counterparts, which were estimated to be 130 mAh/g and 67 mAh/g, respectively. This reduced capacity was explained due to the reduction of lithium diffusion caused by the presence of functional groups. Moreover, Er et al. predicted a lithium ion intercalation capacity of 447 mAh/g for monolayer Ti_3C_2 assuming a double side adsorption [71]. These results suggest that for energy storage

applications it is beneficial to have a non-functionalized Ti_3C_2. Nevertheless, the synthesis of this hasn't been reported to date.

Despite the theoretical calculations, experimental specific capacities show higher values than expected for functionalized non-delaminated and delaminated Ti_3C_2, with an initial specific capacity averaging 250 mAh/g [73][74] and 450 mAh/g [62], respectively. A possible explanation for these results was proposed by Xie et al. [75] who considered that the lithiation of $Ti_3C_2(OH)_2$ occurs under two mechanisms: First, a redox reaction in which the oxidation state of Ti is reduced following equation 2-6 and 2-7 which is responsible for half of the exhibited capacity and, second, the formation of Li-ion layers on top of Ti_3C_2 surface but with no chemical interaction. The occurrence of redox reaction in the surface of Ti_3C_2 is supported by experimental cyclic voltammetry measurements, where Ti_3C_2 evidence a clear pseudocapacitive behavior [76].

$$Ti_3C_2(OH)_2 + 2Li \rightarrow Ti_3C_2O_2Li_2 + H_2 \quad (2\text{-}6)$$

$$Ti_3C_2(OH)_2 + 2Li \rightarrow Ti_3C_2OLi_2 + H_2O \quad (2\text{-}7)$$

When compared to the theoretical capacity of graphite (372 mAh/g), the results of Ti_3C_2 may seem unattractive; however, its near-zero diffusion activation energy for lithium ions (0.07 eV) compared to that for graphite (0.3 eV) is a great advantage which enables fast charging processes with low energy losses [77]. As an example of this, the results of Mashtalir et al. showed that delaminated Ti_3C_2 can exhibits an outstanding capacity of 110 mAh/g at a 36C rate [62]. For this reason, Ti_3C_2 is considered a promising candidate for building fast-charging batteries and supercapacitors [78].

Scientists have devoted their attention to improving the capacity presented by an electrode composed of Ti_3C_2 MXene. First, delaminated Ti_3C_2 is preferred over non-delaminated due to the increased surface area and thus the amount of Li ions that can be stored [62]. In this way, the capacity of MXene can be improved fourfold compared to non-delaminated MXenes; however, problems related to the restacking of MXene monolayers limit its capacity over time [79]. In addition, modification of the

surface chemistry has also been proposed. By a simple vacuum calcination process at 700 °C, Kong et al. demonstrated that the capacity of multilayer MXene was enhanced due to the elimination of -F and -OH groups and the formation of TiO_2 nanoparticles over its surface [74]. Similar oxidation treatments have also been conducted for other MXenes with good results [80]. Finally, composite electrodes with Ti_3C_2 have also been explored to avoid the previously mentioned problems. For example, to reduce the restacking of MXene monolayers, Ti_3C_2 has been composited with other nanomaterials such as graphene [81] or MoS_2 [82], while, in order to increase its capacity, composites have been explored with materials that form alloys with lithium such as Sn [83] and especially Si, where MXene acts as a conductivity enhancer and mechanical buffer.

2.3.3 Ti_3C_2 - silicon electrodes

Combining silicon and Ti_3C_2 MXene to produce composite electrodes brings several advantages to ameliorate the aforementioned challenges faced by both materials separately. However, the idea of using them together is relatively new. In this section, the main works related to the synthesis of Ti_3C_2-Si composites are discussed and summarized in Table 2-1.

In 2018, the first Ti_3C_2-Si composite electrode was reported by Kong et al., where they used a multilayer Ti_3C_2 MXene produced by HF etching and 40 nm silicon nanopowder [84]. The Si content was only 13 wt.%, but still showed a high initial capacity of 880 mAh/g and 188 mAh/g after 150 cycles at a discharge rate of 0.2 A/g. This first result, although far from ideal, experimentally demonstrated that Ti_3C_2 acts as a buffer for the expansion of silicon anodes, which, compared to the composite electrode, exhibited no capacity after 30 cycles. The following year, two other publications using the same synthesis process but with higher silicon content and Ti_3C_2 were reported with 1137 mAh/g after 100 cycles [85] and 550 mAh/g after 500 cycles [86] at a discharge rate of 0.5 A/g and 0.1 A/g, respectively.

The following works focused their attention on the synthesis of Ti_3C_2-Si via different synthesis methods to improve the bonding between the two. Hui et al. [87] proposed a method to grow chemically bonded Si on Ti_3C_2 by a low temperature

magnesiothermic reduction of the SiO_2 modified Ti_3C_2 particles. The synthesized composite electrode was electrochemically tested showing an initial specific capacity of 1849 mAh/g at 0.1 A/g and a decent long-term cycle specific capacity of 973 mAh/g after 800 cycles at a high discharge rate of 1 A/g. In addition, Xia et al. proposed a structure in which porous silicon nanospheres (PSNs) were wrapped by Ti_3C_2 sheets [88]. This was obtained by modifying the surface of PSN with poly-methyl methacrylate (PMMA), which would be spontaneously wrapped by Ti_3C_2 sheets due to the strong interaction between PMMA and Ti_3C_2. The synthesized structure showed an initial capacity of 2077 mAh/g at a discharge rate of 0.2 A/g and a capacity of 1154 mAh/g after 2000 cycles at the same discharge rate. Finally, using the same electrostatic assembly principle, Zhang et al. synthesized a sandwich-like structure by amine functionalization of Si nanoparticles [89]. Cycling results performed at a discharge rate of 0.3 A/g showed an initial capacity of 1181 mAh/g and a capacity of 644 mAh/g after 100 cycles, respectively. These investigations demonstrated that higher capacities can be obtained in long term cycling experiments by improving the contact and adhesion between Si and Ti_3C_2.

The preparation of Ti_3C_2-Si composite electrodes without binders and conductive agents has also been proposed due to the high conductivity of Ti_3C_2 and its good ability to restrain silicon expansion. Zhang et al. improved the capability of silicon anodes by mixing Si nanoparticles in a viscous aqueous Ti_3C_2 ink without binders and conductive agents [90]. The 30 wt.% Ti_3C_2 composite showed an initial capacity of 2450 mAh/g at 0.2 A/g and 910 mAh/g at 1.5 A/g after 275 cycles. Similarly, inspired by Zhang's results, Sarang et al. also used Ti_3C_2 MXene as a conductive additive but with the goal of identifying the lowest amount of Ti_3C_2 that would not impair the electrode's specific capacity [91]. They found that an electrode composed of only 4 wt.% Ti_3C_2 mixed with 16 wt.% binder could allocate 80 wt.% silicon with good results. The prepared electrode exhibited an initial capacity of 3040 mAh/g at 0.3 A/g and kept 720 mAh/g capacity after 200 cycles at 1.5 A/g, which demonstrates the benefits of Ti_3C_2 MXene as an enhancer of silicon capacity and cyclability.

Table 2-1. Summary of Ti_3C_2-Si anode composite works

Composite technique	Materials		Electrode characterization			Electrochemical results			Ref.
	Silicon size (nm)	MXene production	Anode Composition	Thickness (μm)	Loading mass (mg/cm^2)	Initial capacity (mAh/g)	Long-term cycle capacity (mAh/g)	% First Coulombic Efficiency	
Manual mixing	80	HCl - LiF delaminated	Silicon 70% Ti_3C_2 30%	23	0.9	2450 at 0.2 A/g	910 at 1.5 A/g after 275 cycles	81%	[90]
	60	HCl - LiF delaminated	Silicon 80% Ti_3C_2 4% Na-alginate 16%	9	0.7	3040 at 0.3 A/g	720 at 1.5 A/g after 200 cycles	80%	[91]
Ultrasonic mixing	40	HF non delaminated	Silicon 13% Ti_3C_2 67% CMC 10% Carbon black 10%	-	0.7	880 at 0.2 A/g	188 at 0.2 A/g after 150 cycles	69%	[84]
	100	HF TMAOH intercalated	Silicon 21% Ti_3C_2 44% Na-alginate 15% Carbon black 20%	-	1.3	1790 at 0.5 A/g	1137 at 0.5 A/g after 100 cycles	74%	[85]
	-	HCl - LiF delaminated	Silicon 50% Ti_3C_2 50%	-	-	450 at 0.1 A/g	550 at 0.1 A/g after 500 cycles	61%	[86]

Electrostatic/ interfacial assembly	500	HCl - LiF delaminated	Silicon 61.5% Ti_3C_2 8.5% PVDF 10% Carbon black 20%	11.4	1	2077 at 0.2 A/g	1154 at 0.2 A/g after 2000 cycles	80%	[88]
	50	HF non delaminated	Silicon 60% Ti_3C_2 20% PVDF 10% Carbon black 10%	-	-	1181 at 0.3 A/g	644 at 0.3 A/g after 100 cycles	72%	[89]
Magnesio-thermic reduction	40	HF delaminated TMAOH	Silicon 23% Ti_3C_2 37% PVDF 20% Carbon black 20%	4.4	-	1849 at 0.1 A/g	973 at 1 A/g after 800 cycles	61%	[87]
Covalent anchoring	40	HCl - LiF delaminated	-	9	1.2	3500 at 0.2 A/g	1672 at 1A/g after 200 cycles	71%	[92]

(*) Capacity was recalculated when the results were given in respect to only silicon mass for comparison purposes.

3. Experimental

3.1 Materials and electrode characterization

The multilayer Ti_3C_2 MXene, Si and porous Si powders were analyzed to obtain size, morphology and chemical composition information using different characterization techniques, which are summarized in Table 3-1.

Ti_3C_2 powder was provided by colleagues from Ningbo Institute of Materials Technology and Engineering of China. The synthesis process followed has been previously described in detail in [93]. As explained there, commercial Ti_3AlC_2 powder was used as precursor, which was immersed and stirred for 24 hours in a 40% HF solution (0.1 g/mL) at room temperature. Then, the solution was washed several times with deionized (DI) water until a pH above 6 was reached. Finally, the powder was separated by centrifugation followed by filtration under vacuum conditions and dried at room temperature for 24 hours in a vacuum oven.

Additionally, 99% Si porous powder was purchased from Nanoshel UK (Stock number: NS6130-01-143) with a particle sized below 50 nm while 98% Si crystalline nanopowder with a particle size also below 50 nm synthesized by laser from the vapor phase was purchased from Alfa Aesar (Cas. 7440-21-3).

Table 3-1.. Techniques employed for powder characterization

Characterization technique	Porous Silicon	Silicon powders	Ti_3C_2
Scanning electron microscopy (SEM)	X	X	X
Dynamic light scattering (DLS)		X	X
Electron dispersive X-ray (EDS)			X
X-ray diffraction (XRD)			X

The sample preparation of Ti_3C_2 for scanning electron microscopy (SEM) consisted of dispersing 1 mg Ti_3C_2 powder in 4 mL of ethanol solvent in order to avoid possible oxidation of its surface for 15 minutes under sonication. Then, a few drops of the colloid were drop casted onto a Si (100) wafer and dried for a few minutes under ambient conditions. Subsequently, the Si wafer was stored in a glovebox with argon

(Ar) environment until the measurement was performed. In the case of the silicon nanopowder, the same procedure was followed but using deionized (DI) water as solvent due to the hydrophilicity of Si nanoparticles and a carbon grid as substrate for the drop casting step. SEM images were taken at different magnifications using a Hitachi S-4800 SEM with an accelerating voltage of 20kV, 5kV and 30kV for Ti_3C_2, porous Si nanopowder and Si nanopowder, respectively. For the energy dispersive X-ray spectroscopy (EDS) performed on Ti_3C_2 powder, an acceleration voltage of 15 kV was used for the same sample. The analysis was averaged over 5 measuring spots of the sample where Ti_3C_2 powder was visible.

Dynamic light scattering (DLS) was used to quantitatively measure the particle size distribution of the powders dispersed in water. The measurements were performed on a Malvern Zetasizer Nano instrument (ZS ZEN 3600). Ti_3C_2 and Si powder were dispersed for 15 minutes under ultrasound in DI water at a concentration of 10 mg/L. Few drops from the supernatant were poured into a polystyrene cuvette and three measurements were performed consecutively. The mean size was obtained. Based on the changes in scattered light, the DLS technique calculates the particle size assuming a spherical particle shape. This must be considered when interpreting the results for laminated materials such as the Ti_3C_2.

X-ray diffraction (XRD) analysis was performed to analyze the crystal structure of Ti_3C_2 MXene on a Siemens D5000 X-ray diffractometer using a grazing incidence configuration. The powder sample was scanned with a step size of 0.02° and a dwell time of 3 seconds per step between incidence angles from 5° to 90°. During data processing, the K-α2 radiation and background were removed to clearly see only the peaks related to Ti_3C_2.

Finally, characterization of the prepared electrodes was also performed. Optical microscope (VW-9000 Keyence) and SEM images (accelerating voltage of 20 kV) were obtained to characterize the surface morphology of the prepared electrodes.

3.2. Electrodes preparation

Eight electrodes of different composition and materials were prepared as shown in Table 3-2. The procedure to prepare them follows the description of the diagram in Figure 3-1.

Table 3-2. Composition of electrode slurries

Anode	Solid content (g)	% Solid content composition				Slurry concentration (g/mL)
		Silicon	MXene/ Graphite	Carbon black	CMC	
Silicon nanoparticles	1.06	90%	0%	5%	5%	0.20
MXene	1.06	0%	90%	5%	5%	0.31
Graphite	1.399	0%	90%	5%	5%	0.31
Silicon 80/ MXene 20	1.22	72%	18%	5%	5%	0.20
Silicon 60/ MXene 40	1.22	54%	36%	5%	5%	0.31
Silicon 20/ MXene 80	1.22	18%	72%	5%	5%	0.31
Silicon 60/ Graphite 40	1.22	54%	36%	5%	5%	0.31
Porous Silicon	1.22	90%	0%	5%	5%	0.31

First, the mass of each powder was weighed on an analytical Sartorius balance (CPA124S, resolution of 0.1 mg) and then mixed manually in a 5 mL vial. Afterwards, a solution of previously prepared carboxymethyl cellulose binder (CMC) dispersed in DI water (1.5 g/mL) was added and mixed manually until the powder was no longer visible. Then, to homogenize the slurry, a hydrodynamic disperser (Miccra D-8) was used at a speed of 23500 RPM for 20 minutes. Afterwards, the slurry was deposited on a Cu foil substrate (12 μm thickness) by blade coating technique (Zehntner – ZAA

2300). The gap height was set to 50 μm and a coating speed of 5 mm/min was used during the coating process. The coated Cu foil was then allowed to dry under ambient conditions for a few minutes and subsequently transported to a lab oven (Heraeus) where it was left to dry overnight at 80°C.

At the following day, the Cu foil was removed from the oven and 11 mm diameter electrodes were cut with a high precision electrode punching tool (EL-Cut). The mass of the electrodes was measured three times for three different electrodes on the analytical balance. The mass value reported for each electrode composition in the following work corresponds to the average value of three measurements subtracted by the mass of an uncoated 11 mm diameter Cu foil (10 mg). Finally, the electrodes were dried again for 6 hours at 80°C to remove any remaining traces of trapped water and then stored in a GS glove box under Ar environment with controlled low water and oxygen content (0.2 ppm and 0 ppm, respectively).

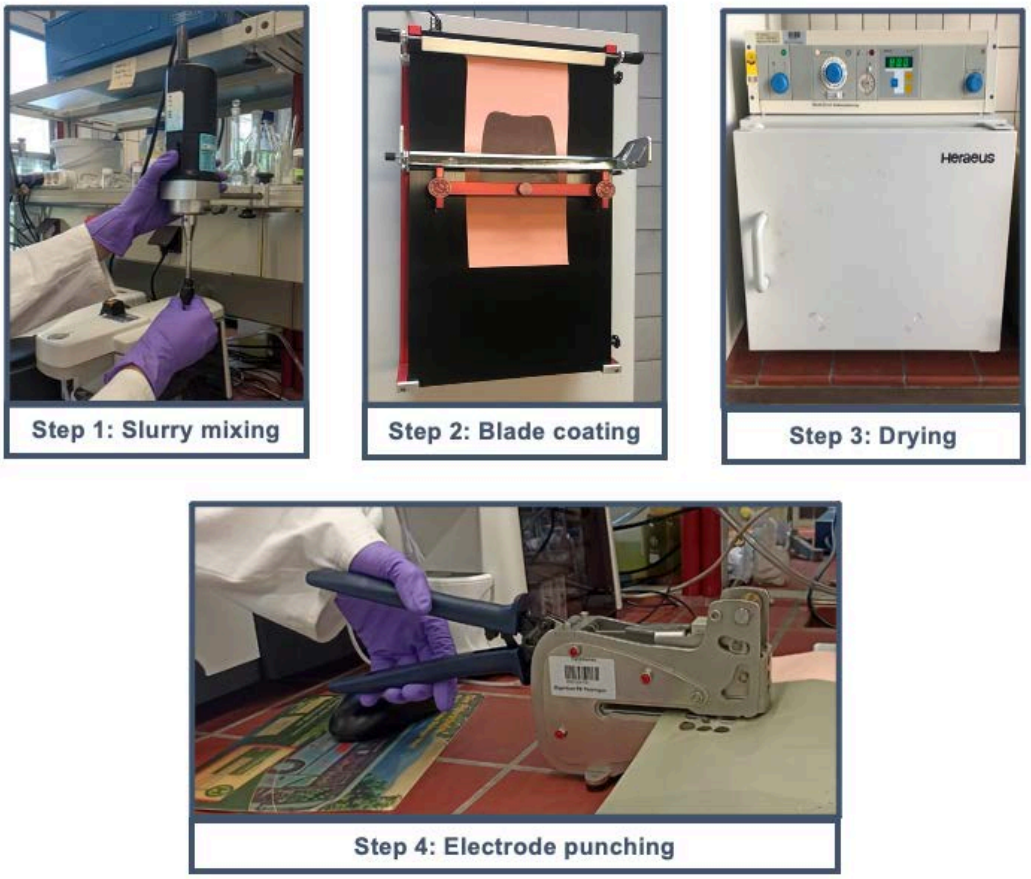

Figure 3-1. Electrode preparation procedure

3.3. Coin cell assembly

To study the electrochemical performance of the previously prepared electrodes, three coin cells for each electrode were assembled. A schematic representation of the components and their order of assembly within the coin cells is shown in Figure 3-2. Lithium metal (Sigma-Aldrich CAS No. 7439-93-2) was chosen as counter electrode and 12 mm diameter circular Li electrode were punched and placed in the center of the negative case of a CR 2025 coin cell. A 16.5 μm diameter Whatman fiber glass separator (CAT No. 1822-070) was then placed over the lithium to act as an electrical isolator between the two electrodes. Next, 120 μL of the electrolyte (Sigma-Aldrich) composed of 1M LiF_6 salt dissolved in a mixture of ethylene carbonate and diethyl carbonate (EC: DEC 50:50 v/v) was added, and then the working electrode was placed backwards and aligned with the Li metal. To promote uniform force distribution and good contact between the cell components when closing the cell, a 15.5 mm stainless steel spacer and a wave spring were placed on top of the working electrode. Finally, the cell was sealed with an MSK-110 hydraulic crimping machine applying a force of 80 kg/cm^2. The whole assembly process was performed inside a GS glovebox in an Ar environment.

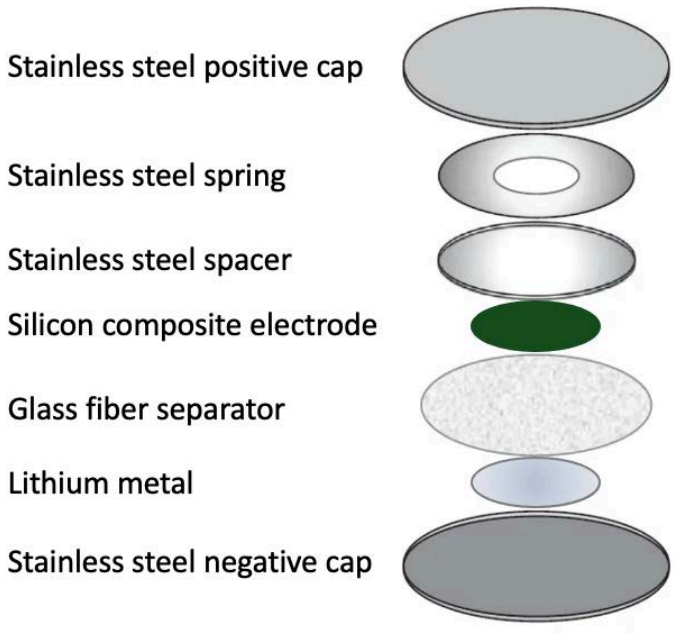

Figure 3-2. Diagram of a half-cell lithium-ion battery configuration. Adapted from [94]

3.4 Electrochemical cycling procedure

The galvanostatic cycling procedure was carried out using a VPM3 Biologic potentionstat. The cycling procedure consisted of constant current cycles between a voltage range of 10 mV to 1.2 V with the first three cycles performed at charge-discharge rates of C/10, C/5 and C/2 in order to promote a homogeneous formation of the solid electrolyte interface (SEI) layer, followed by 100 cycles at a rate of 1C. Before starting the cycling procedures, the cell was at rest for 12 hours to promote good wetting of the separator and avoid voltage losses. The theoretical specific capacities of Si (3579 mAh/g) and graphite (372 mAh/g) were used to calculate the corresponding currents. In the case of Ti_3C_2, due to the differences between theoretical and experimental results observed in the literature, 250 mAh/g was used as the specific capacity, since it was the experimental capacity observed in most publications. Following the above mentioned and based on the mass of the electrodes (not including the current collector) and their composition of each material, the charging current was determined using the equation 3-1 and the obtained results are summarized in Table 3-3.

$$\text{Current} = \frac{(\text{electrode mass} - 0.01\ \text{mg}) * \sum \text{Specific capacity}_i * \text{Material}_i\ \text{wt.}\%}{Cycle\ duration\ (in\ hours)} \quad (3\text{-}1)$$

Table 3-3. Electrodes charge-discharge rates

Anode	Theoretical capacity (mAh/g) (*)	Charge-discharge rates (mA)			
		C/10	C/5	C/2	1C
Silicon nanoparticles	3220	0.23	0.46	1.15	2.3
MXene	225	0.02	0.04	0.1	0.2
Graphite	335	0.03	0.06	0.15	0.3
Silicon 80/MXene 20	2645	0.2	0.4	1	2
Silicon 60/MXene 40	2025	0.2	0.4	1	2
Silicon 20/MXene 80	830	0.1	0.2	0.5	1
Silicon 60/Graphite 40	2065	0.23	0.46	1.15	2.3
Porous Silicon	3220	0.26	0.52	1.3	2.6

(*) Include the mass of binder and conductive agent for the calculations

Differential capacity analysis (dQ/dV vs V) figures were constructed by plotting the additional capacity obtained every 20 mV (dQ) divided by 0.02 (dV) against the voltage. To compare, for a given electrode, peaks between cycles and avoid the effect of capacity fading, the capacities for each cycle were normalized to the capacity observed in the last cycle (100^{th} cycle at 1C) by multiplying the capacities by a factor to make all the capacities equal.

The hysteresis was obtained by calculating the difference between the delithiation average operating voltage and the lithiation average operating voltage. These operating voltages were obtained by integrating the curve voltage vs capacity (energy of the system) and dividing it by the total capacity exhibited during that cycle.

Potentiostatic electrochemical impedance spectroscopy (PEIS) characterization was performed to investigate the electrochemical processes occurring inside the cell prior to the galvanostatic cycles. The measurements were performed at open circuit voltage (OCV) between a frequency range of 200 kHz to 100 mHz using a 10 mV amplitude. The test was run 5 times on each electrode to verify reproducibility of the observed results.

4. Results and discussion

4.1. Materials characterization

4.1.1 Silicon nanopowders

In the following experiments, two commercial silicon powders: porous Si nanoparticles (p-SiNP) and non-porous Si nanoparticles (SiNP) from different suppliers were analyzed. According to the suppliers, both powders should exhibit 50 nm particle size. Figure 4-1 shows SEM images of both materials which can be analyzed to confirm their morphology and particle size.

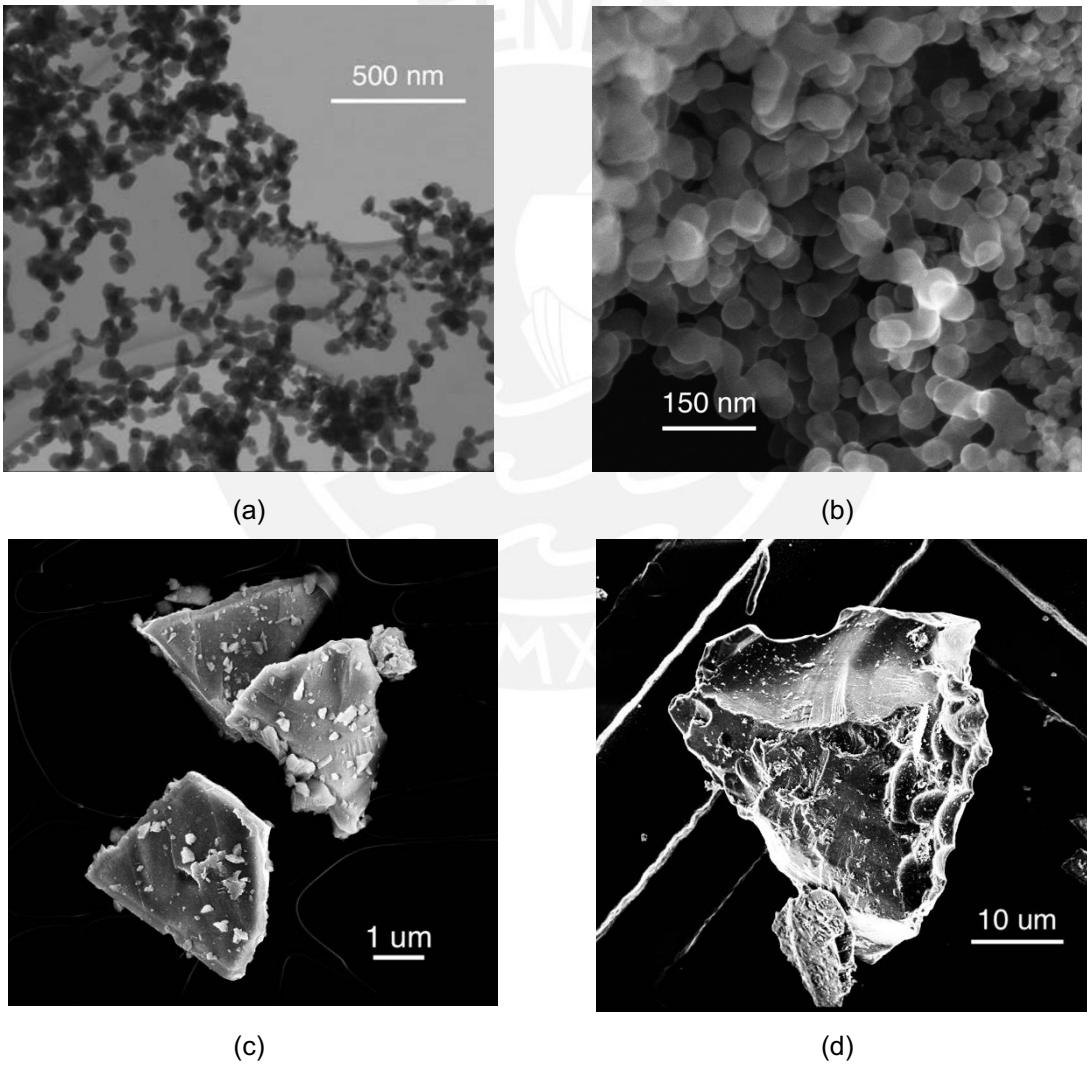

Figure 4-1. SEM images of (a), (b) silicon nanopowder and (c), (d) porous silicon nanopowder.

By comparing the SEM images of SiNP and p-SiNP, several differences are identified. Figure 4-1a and Figure 4-1b confirm that SiNP particle size is on average 50 nm, in agreement with the value reported by the supplier. Whereas p-SiNP (Figure 4-1c and Figure 4-1d) presents particles in the microscale range with a particle size below 40 μm. In addition, both exhibit differences in their morphology. SiNP presents a round spherical shape in agreement with the morphology published in the literature for silicon nanoparticles synthesized by laser from vapor phase [95]. Some degree of aggregation of SiNP particles is also observed. On the other hand, p-SiNP presents a tetrahedral and conical shape with no visible porosity over its surface. These observations differ from the expected properties reported by the supplier of pSiNP.

A visual inspection between the two powders shown in Figure 4-2 provides additional qualitative information on particle size. As expected from a nanoparticle-sized powder, the SiNP exhibits a yellow color compared to silicon bulk material (gray) and a larger volume is occupied due to electrostatic repulsive forces between nanometer-sized particles. None of these properties is observed in p-SiNP.

Figure 4-2. Image of 100 mg Si nanopowder (left) and porous Si nanopowder (right) in a 5 mL vial

Quantitative information on particle size was also obtained by dynamic light scattering (DLS) and is shown in Figure 4-3. The average particle size of SiNP in DI

water was found to be 332 nm. Additionally, the particle size frequency distribution of SiNP show a bimodal distribution with a first broad peak between 100 to 1000 nm and a second one from 2 to 7 μm (right tail in the particle size distribution) This result differs from the previous values observed by SEM, which is explained mainly due to agglomerated particles considered as one during the DLS measurement. Similar studies were not performed for p-SiNP because the particle size result previously observed by SEM makes these particles unsuitable for the DLS technique (below 10 μm particle size).

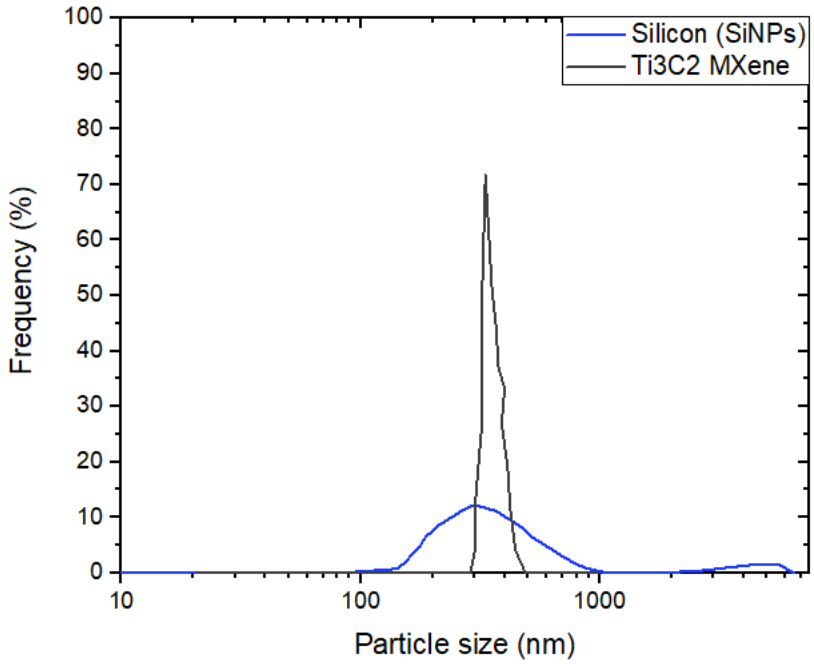

Figure 4-3. Particle size measured by SEM of silicon nanoparticles (blue) and Ti_3C_2 (gray)

Particle size greatly influences the electrochemical performance of silicon anodes and therefore, due to the differences shown against the expected characteristics of p-SiNP, the experiments were focused mostly on SiNP.

4.1.2. Ti_3C_2 MXene

Ti_3C_2 multilayered MXene characteristics were also investigated as in the case of silicon nanopowder. The micrographs shown in Figure 4-4 confirm a multilayer accordion structure, as usually reported in the literature on MXene powder [60]. This

structure shows evidence of the successful etching of Al from the precursor (Ti_3AlC_2 MAX Phase). In addition, the particle size ranges from 1 to 5 μm composed of multilayer particles that consists of several Ti_3C_2 monolayers. The spacing between these layers is about 100 nm as shown in Figure 4-4 b. This is an interesting feature due to the possibility of silicon nanoparticles to fit in between layers during the composite preparation.

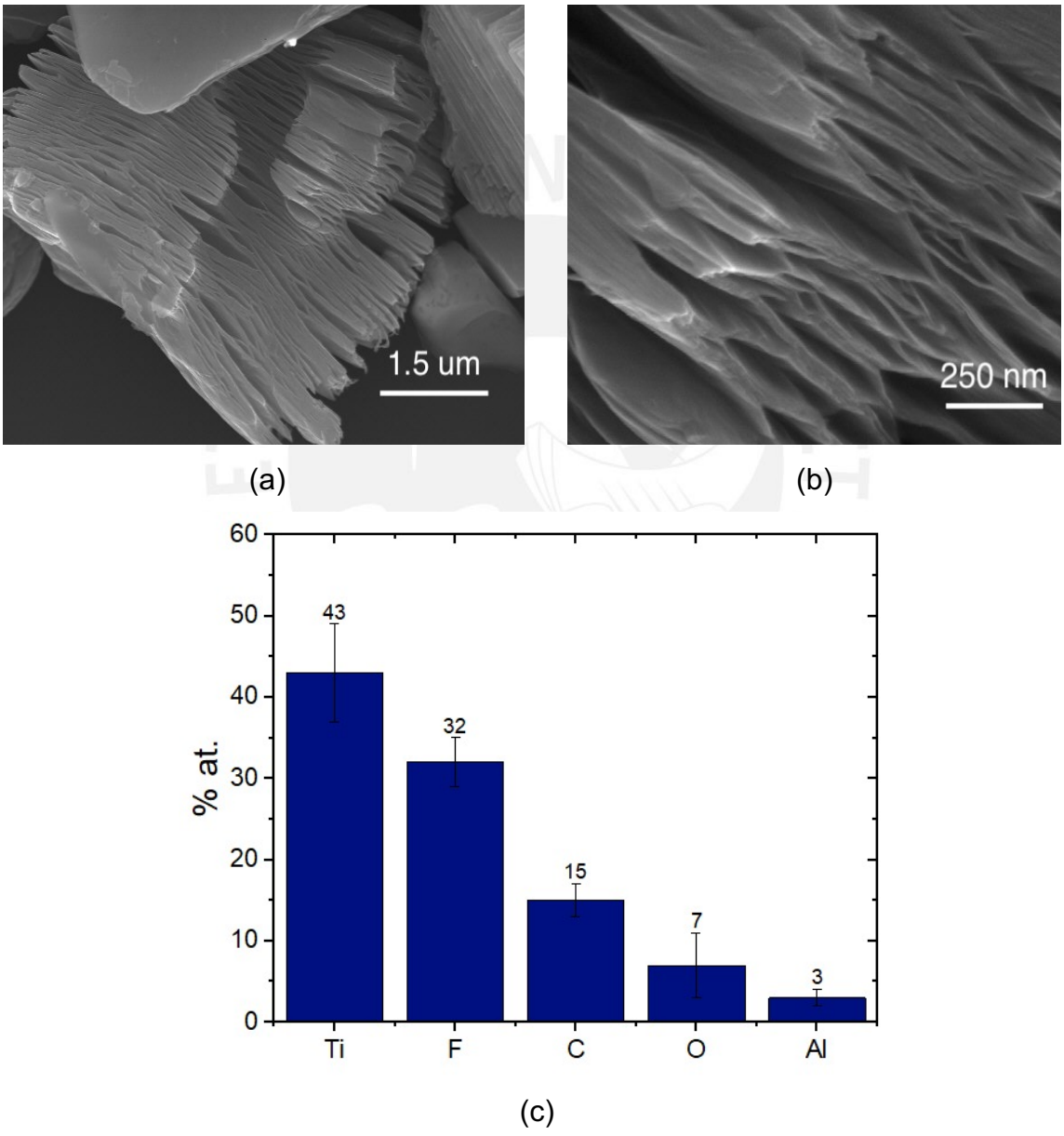

Figure 4-4. SEM images of (a) Ti_3C_2 low magnification and (b) high magnification. (c) EDS analysis of the elemental composition of Ti_3C_2

Quantitative particle size analysis by DLS shows a mean particle size of 400 nm with a narrow peak between 300 to 500 nm (Figure 4-3). These results differ from the particle size observed in SEM images, which could be explained by the rapid sedimentation of the fraction of large-size particles during sample preparation for DLS. It is known that, in a suspension, large particles tend to settle quickly compared to small particles, which remain suspended due to Brownian motion. Therefore, the particle size of Ti_3C_2 reported by DLS measurements might be related only to the fraction of particles on the nanoscale range. Another source of differences may be due to the assumption of a spherical shaped particle when calculating the particle size using the DLS technique. This assumption may not be suitable for laminated 2D materials such as Ti_3C_2.

The chemical composition of Ti_3C_2 MXene is of great interest to study the removal of the aluminum atoms from the structure due to etching of the precursor, the concentration of other elements (Ti, C) as well as the concentration of F and O elements that can be attributed, in part, to the functional groups present on the surface of the powder. Energy dispersive X-ray spectroscopy (EDS) result is shown in Figure 4-4c. As expected from the synthesis process, the presence of aluminum (Al) is only of 3 at. % which confirms the selective etching of the Al layer of the precursor Ti_3AlC_2 MAX Phase. In addition, fluorine and oxygen represents 32 at. % and 8 at. % of the analyzed elements in the powder composition. These two elements result from the chemical wet etching process that the precursor Ti_3AlC_2 underwent in a high concentrated HF solution. During this process, the Al reacts with the HF to form AlF_3 crystals and, due to the charge imbalance left in the material, titanium (Ti) atoms on the surface bond with -F, -O, and -OH ions present in the etching solution. This leads to the synthesis of a functionalized $Ti_3C_2T_z$ with T_z referring to the presence of the functional groups on the structure. Moreover, the Ti:C atomic ratio (3:1) is lower than expected for Ti_3C_2. This difference can be explained by an overexcitation of the C atoms at the accelerating voltage used. In summary, it can be concluded from the previous results that an etching process with a high HF concentration leads to the high presence of the -F functional group.

Finally, the crystal structure of the Ti_3C_2 powder was studied by X-ray diffraction analysis (XRD) as shown in Figure 4-5. The most intense diffraction peak related to the Ti_3AlC_2 MAX phase located at 39.4° is no longer visible, which also confirms the etching of the Al layer and a correct synthesis of Ti_3C_2 [60]. In addition, an increase of the c lattice parameter is observed due to the change of the crystalline plane (002) at 8.7° with respect to the usual precursor Ti_3AlC_2 peak at 9.6°. This change is explained by the presence of mainly -F and -O functional groups as reported in previous theoretical XRD peak calculations for Ti_3C_2 of different functional groups [60]. The new c lattice parameter corresponds to a distance between monolayers of about 1 nm. Likewise, the other peaks observed correspond to those present in Ti_3C_2 functionalized with -F and -O. The most intense ones are related to the -F functional group. The latter is in agreement with the results observed by EDS. At last, no traces of other phases, which could have arisen from the synthesis process or the oxidation of Ti_3C_2 such as TiO_2 anatase ((101) - 25.3°), TiC ((111) - 38° and (200) - 41°) or graphite ((002) - 26.5°) are observed in the diffractogram.

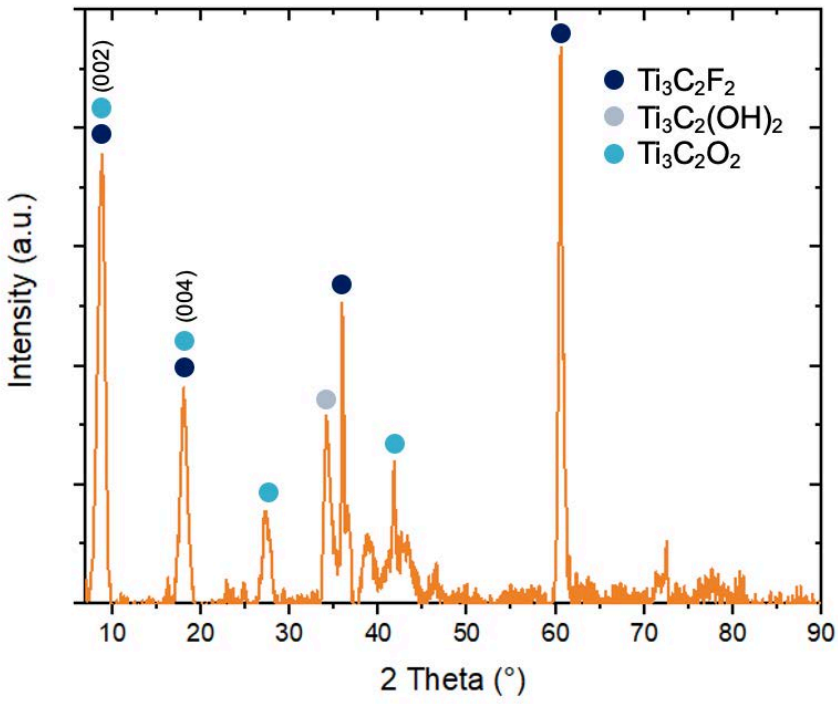

Figure 4-5. XRD results for Ti_3C_2 MXene. The theoretical peaks used correspond to the calculations performed in [96]

Based on the previous experiments, it can be concluded that the powder fulfills the criteria of a Ti_3C_2 multilayer material.

4.2. Electrodes characterization

The mass loading of the prepared electrodes following the procedure described previously (Section 3.2) is shown in Table 4-1. It can be observed that different loading masses were obtained for each composition even though the same procedure and the same blade thickness (50 μm) were used for the coating.

Table 4-1. Loading mass and theoretical capacity of fabricated electrodes

Anode	Code	Loading mass (mg)		Theoretical capacity (mAh/g)
		M	SD	
Silicon nanoparticles	Si	0.73	0.11	3220
MXene	MX	0.93	0.05	225
Graphite	GP	0.87	0.07	335
Silicon 80/ MXene 20	SiMX20	0.74	0.09	2645
Silicon 60/ MXene 40	SiMX40	1.00	0.05	2025
Silicon 20/ MXene 80	SiMX80	1.14	0.05	830
Silicon 60/ Graphite 40	SiGP40	1.11	0.07	2065
Porous silicon	PSi	0.81	0.06	3220

The lower loading mass of the samples with high silicon content (Si and SiMX20) is explained by the need to use an additional 2mL DI water to properly disperse the silicon nanoparticles which, as shown in Figure 4-2, present a low density in powder form. This property of silicon nanoparticles makes it particularly difficult to obtain a homogeneous slurry to produce high loading mass electrodes. This is evidenced in

the standard deviation values obtained for Si and SiMX20 electrodes, which are the highest of all electrodes. In the case of the composite SiMX40, SiMX80 and SiGP40 electrodes, the loading masses obtained were higher than 1 mg in contrast to the lower masses obtained for their respective non-composite MX, GP and PSi electrodes. These results suggest that there is good compatibility between the materials during slurry mixing that allows the fabrication of dense high-loading mass electrodes.

Optical microscopy images of the prepared electrodes are shown in Figure 4-6. As can be seen in Figure 4-6a, the pure Si anodes present a homogeneous surface but with visible cracks. Previous reports have shown that electrodes processed in aqueous media tend to form cracks during the drying procedure due to capillary forces exhibited during shrinkage [97]. Therefore, the high-water content required for pure Si slurry preparation is the main cause for the observed cracks. This same behavior is observed for SiMX20 (Figure 4-6f).

Moreover, SiMX40 (Figure 4-6e) and SiGP40 (Figure 4-6g) also show cracks but in a smaller amount. This could be caused by an inhomogeneous distribution of the binder in composite electrodes with high Si content due to lack of binder to cover its high surface area. This reasoning may explain why no visible cracks are observed in SiMX80 (Figure 4-6d), Ti_3C_2 (Figure 4-6b) or graphite (Figure 4-6c) electrodes even though the same preparation procedures were applied. On the other hand, bright orange regions are observed on the surfaces of the non-composite electrodes, particularly in Ti_3C_2 electrode (Figure 4-6b), which corresponds to areas where the copper foil has not been completely coated with the material particles. Since the slurry was prepared with an equal ratio of powder mass: DI water volume for the electrodes, it is expected that the volume occupied by the denser powder will be smaller. That is the case of Ti_3C_2 which has a density of 4.21 g/cm^3. Thus, the preparation of Ti_3C_2 - Si composites allowed to obtain a good compromise between a minimum cracks formation and a proper Cu foil coating with active material.

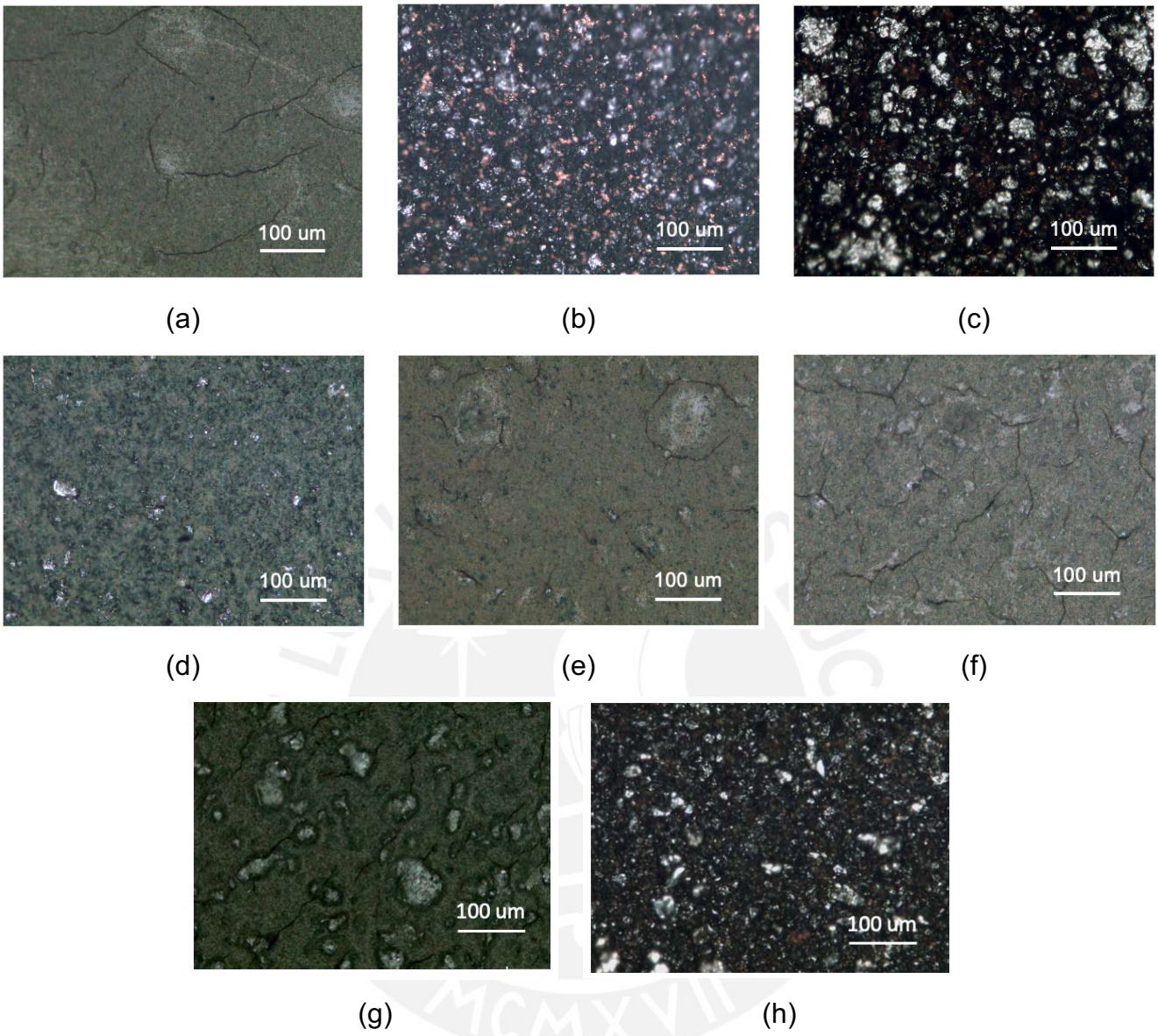

Figure 4-6. Optical microscopic images taken of (a) Si, (b) Ti_3C_2, (c) graphite (d) SiMX80 (e) SiMX40 (f) SiMX20 (g) SiGP40 and (h) porous Si anodes at a 500x magnification.

SEM micrographs of the SiMX40 composite were obtained to analyze the interaction of silicon and Ti_3C_2 particles on the electrode and are shown in Figure 4-7. As discussed previously, it is observed that Si nanoparticles are covering most of the electrode volume due to its low dense nature in comparison with Ti_3C_2. The red circles in Figure 4-7a highlight some areas where Ti_3C_2 particles are visible in the surface. A magnification of two of them can be observed in Figure 4-7b and Figure 4-7c. From these images it is possible to observed that most of the silicon

nanoparticles cover the surface of the multilayer Ti_3C_2, with some of them inserting between the layers near Ti_3C_2 borders. These results resemble the structure obtained in [84] by ultrasonication, where the characterization confirmed the intercalation of Si nanoparticles between Ti_3C_2 layers. However, addition characterization such as cross-section view of the electrodes is required to confirm the full insertion of Si nanoparticles.

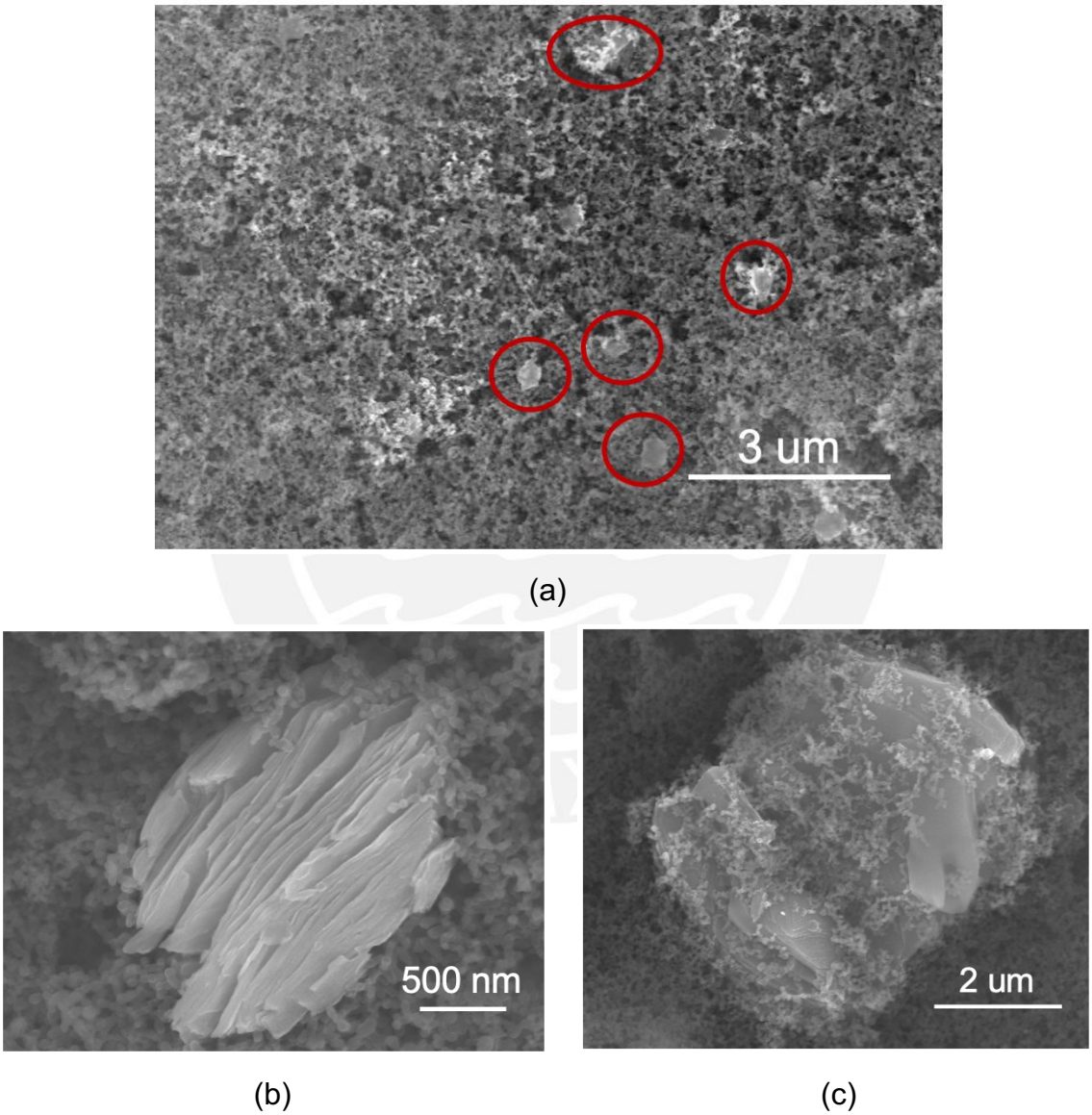

Figure 4-7. SEM images of (a) SiMX40 surface, (b-c) Ti_3C_2 particles in the structure. Red circles highlight the zones were Si and Ti_3C_2 are in contact

Finally, the reproducibility of the electrode preparation procedure was evaluated by comparing the cycling results of SiGP40 electrodes belonging to three different production batches. As shown in Figure 4-8, the three batches have a similar specific cycling capacity during the cycles, which confirms the reliability of the preparation procedure. Also, it is observed that the standard deviation between the results of cells from a given batch is minimal (5% of the mean value). As the cells within a batch were built with electrodes randomly punched from the coated Cu foil, it can also be stated that the slurry coating is homogeneous.

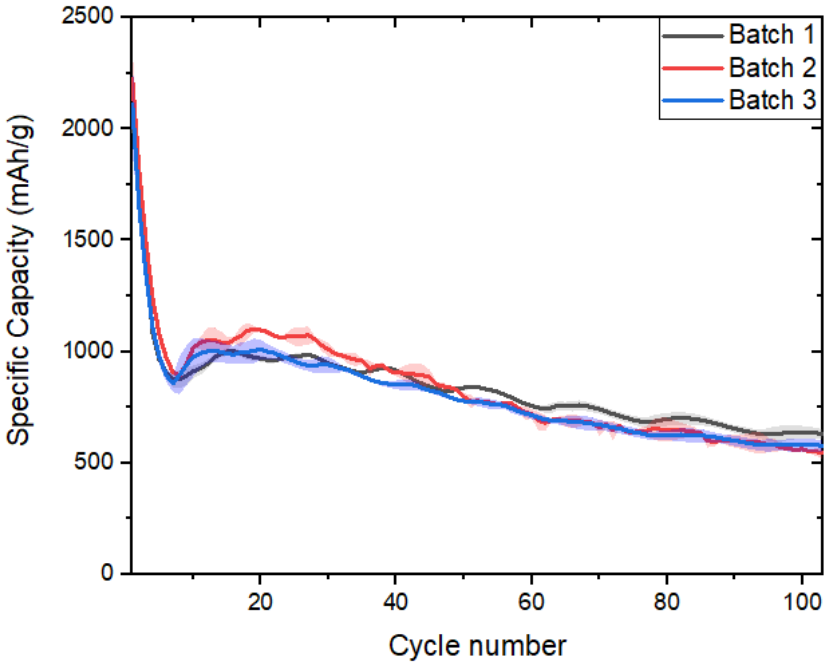

Figure 4-8. Cycling results of three different SiGP40 batches at 0.2 mA/g

4.3 Electrochemical performance

4.3.1 Electrochemical results of Si and MXene

The electrochemical behavior of the Si nanoparticles and Ti_3C_2 used to build the composite electrodes was first studied to determine their performance on their own. Figure 4-9 shows the lithiation/delithiation profiles of Ti_3C_2 MXene where a predominantly linear behavior caused by the pseudocapacitive behavior if Ti_3C_2 is observed and only some small plateaus are visible during the first cycle (gray lines). Furthermore, a large difference is observed between the capacity during the first

lithiation (340 mAh/g) and delithiation (111 mAh/g) giving an initial coulombic efficiency (ICE) of 33%. Previous work has determined that the initial coulombic efficiency of Ti_3C_2 is of 47% caused by SEI formation and irreversible reactions of the electrochemically active functional groups [98]. The difference with the results presented in this work could be related to a partial delithiation of Ti_3C_2 (Li ions trapped in its structure), since the delithiation cutoff voltage (1.2 vs Li/Li^+) set for the experiments is below the open circuit voltage of the fresh half-cell (1.7 vs Li/Li^+). Figure 4-9 shows that the lithiated capacity during the first cycle from 1.7 to 1.2 V vs Li/Li^+ represents approximately 10% of the entire lithiated capacity (35 mAh/g); thus, validating the above hypothesis. It is important to mention that from an application point of view, this remaining capacity observed at high voltages are of less interest for a full cell battery with Ti_3C_2 as the anode due to the reduction of the voltage difference between the cathode and the anode (cell operating voltage) and, therefore, the lower contribution of it to the total cell energy.

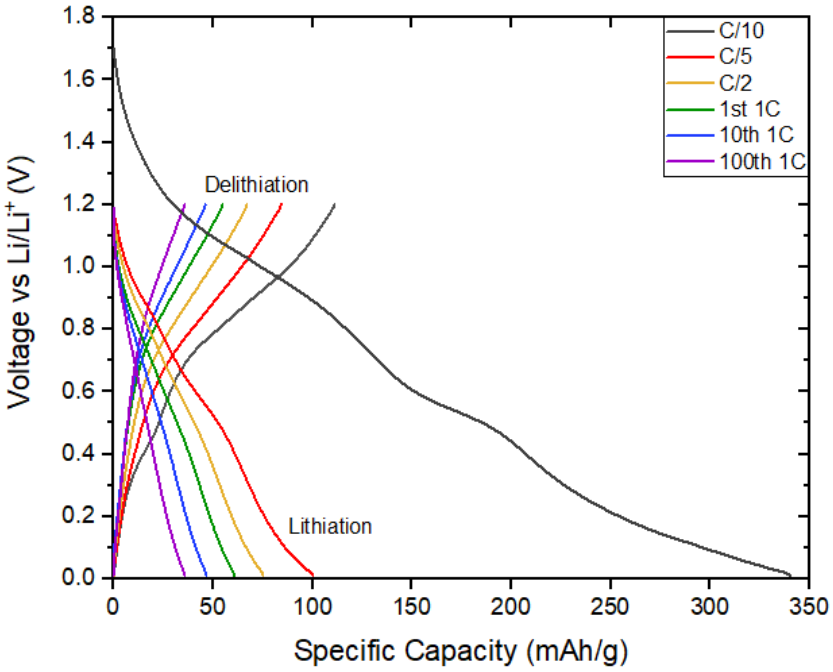

Figure 4-9. Lithiation and delithiation profiles of Ti_3C_2 MXene

Differential capacity analysis was also studied to understand the electrochemical processes occurring during Ti_3C_2 cycling. Figure 4-10 represents the normalized dQ/dV over the voltage vs Li/Li^+ of the first 4 cycles as described in Section 3.4. The

shape of the curves shows that Ti_3C_2 has a pseudocapacitor behavior. During the first lithiation, three peaks are observed. The first peak at 0.03 V is often related to an irreversible reaction of the Super-P carbon black lithiation. Meanwhile, the second peak at 0.54 V may be related to an irreversible side reaction. In addition, the 1.06 V peak has been previously described as an irreversible peak related to the formation of the solid electrolyte interface (SEI). This peak overlaps with a broad peak from 0.74 to 1.16 V that can be related to a reversible faradaic reaction with its observed delithiation counterpart of 0.7 to 1.12 V. As the current cycle rate increases, the previously described peaks disappear and are no longer visible at a cycle rate of 1C. This behavior could be explained by a change in the charge storage mechanism of Ti_3C_2, i.e., at slow cycle rates, the Ti_3C_2 MXene behavior could resemble an intercalation pseudocapacitance mechanism in which Li insertion occurs with slower kinetics, whereas at higher cycle rates, this mechanism could change to a redox/electrical double layer pseudocapacitance in which the reactions occur mainly on the surface of the material.

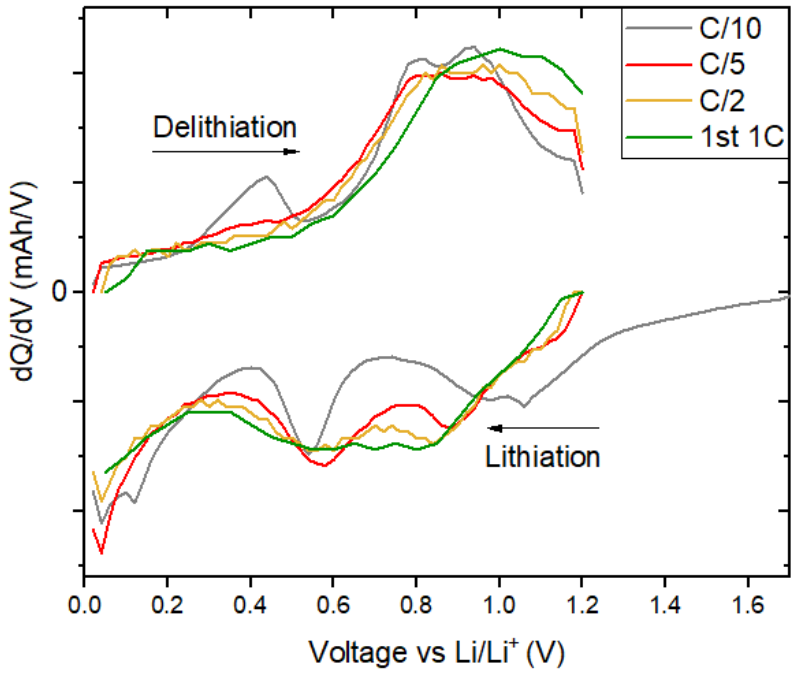

Figure 4-10. Differential capacity analysis of Ti_3C_2

Finally, the long-term cycling performance of multilayer Ti_3C_2 was studied, and the results are shown in Figure 4-11. As it has been explained previously, the initial coulombic efficiency (ICE) of 33% exhibited byTi_3C_2. This metric increases to 90% and 99% after 4 and 12 cycles, respectively, which suggest that the side reactions described previously (SEI formation and active functional groups irreversible reactions) occurs only during the first 4 cycles. Moreover, the delithiation capacity of Ti_3C_2 at the first 1C cycle correspond to a capacity of 55 mAh/g which remains at 36 mAh/g after 100 cycles.

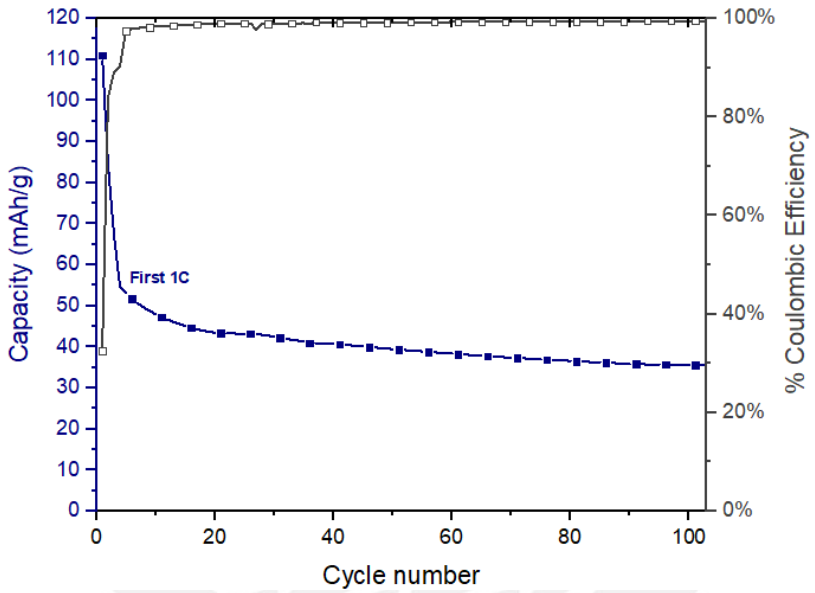

Figure 4-11. Long-term cycling of Ti_3C_2 at 1C rate current

A similar analysis was performed for pure silicon anodes. Figure 4-12 shows the lithiation/delithiation profiles of the prepared silicon nanoparticle anode, where capacities of 2300 mAh/g and 1798 mAh/g are observed during the initial lithiation and delithiation cycles, respectively. Unlike the case of Ti_3C_2 MXene, a complete delithiation process is observed for the Si anode, as its profile increases rapidly once the delithiation capacity reaches 1600 mAh/g. Therefore, the initial low coulombic efficiency, calculated at 78%, is mainly explained by the formation of the SEI layer, which requires a large amount of electrolyte due to the high surface area of the silicon nanoparticles. Moreover, it is observed that the shape of the first lithiation (gray line) is particularly different from that of the following cycles, with a visible

plateau at 60 mV. This is explained by the electrochemical conversion of the non-lithiated crystalline Si into lithiated amorphous Si. This process only occurs during the first cycle, since, at the end of the following delithiation cycles, the Si does not return to its initial non-lithiated crystalline form but is transformed into amorphous Si. In addition, it is observed that the shape of the following lithiation and delithiation cycles show a visible plateau. In particular, the shape of the plateau of the delithiation cycles is different from the result reported by Obrovac et al. [40], which shows a flat plateau behavior during delithiation at around 0.42 V when Si is lithiated previously below 50 mV. As is well known, flat plateaus are related in LIB to kinetically limited electrochemical processes and, therefore, the difference might be explained by the improvement on delithiation kinetics due to nanosized effect.

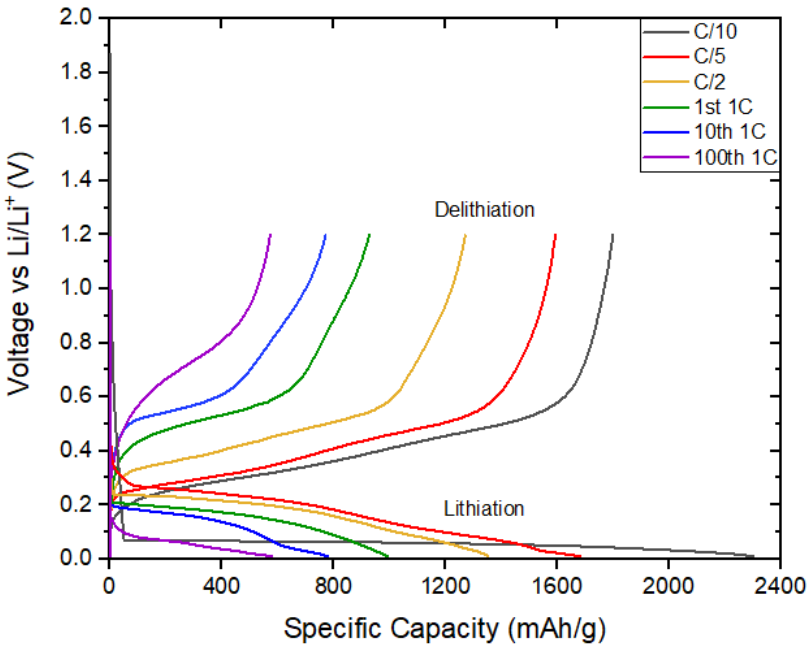

Figure 4-12. Lithiation and delithiation profiles of pure silicon anode

Analyzing the differential capacity shown in Figure 4-13, it can be observed that the initial lithiation plateau described above results in a sharp peak at 60 mV with no other visible peaks. During the following delithiation process, two broad peaks are observed at 0.3 and 0.5 V, the first corresponding to the delithiation of amorphous Si, while the second, to the delithiation of crystalline Si ($Li_{15}Si_4$) and the delithiation of amorphous Si at a higher voltage. In the second lithiation cycle (C/5), three peaks

at 0.01 V, 0.1 V and 0.22 V are observed. The latter two peaks correspond to the lithiation of amorphous Si, while the first is associated with the phase transformation of lithiated amorphous Si to $Li_{15}Si_4$.

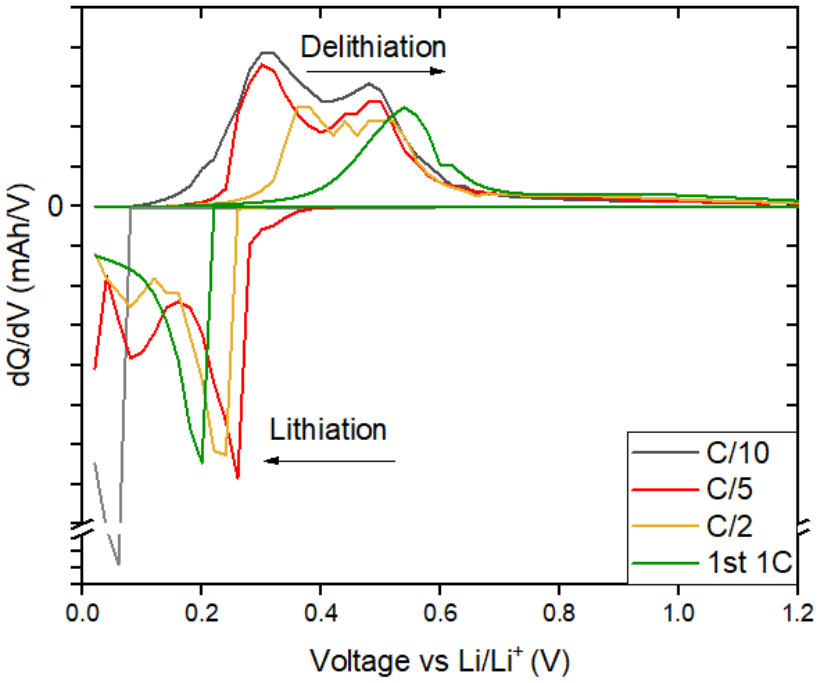

Figure 4-13. Differential capacity analysis of pure Si anodes

The lithiation peaks and their corresponding delithiation peaks described above do not occur at equal voltages, a common Si anode problem known as voltage hysteresis that has a clear impact on charge/discharge energy efficiencies. In addition, a shift of the lithiation and delithiation peaks to lower and higher voltages, respectively, is observed, accompanied by the disappearance of some peaks when the current rate increases and the cell is subjected to long-term cycling. First, the peak at 10 mV disappears quickly and is only visible until the second cycle, which could be caused by overpotential losses as the current increases. As this peak is related to the change from amorphous to crystalline structure, it is reasonable to think that in the following cycles $Li_{15}Si_4$ phase is no longer formed. Secondly, the peaks at 0.1 V (lithiation) and 0.3 V (delithiation) progressively disappear and are no longer visible at the 1C rate. Finally, an increase in the hysteresis effect (refer to Section 3.4 for detail on the calculations) can be observed at long-term cycles These

results show that the hysteresis effect increases from 0.48 V at the first 1C cycle to 0.68 V at the end of 100 cycles. This metric will be further compared with different Si-MXene composites to evaluate the effect of Ti_3C_2 in preventing the degradation of the hysteresis mechanism of Si anodes by reducing Si expansion, since voltage hysteresis is often related to compressive stress suffered by Si electrode [99].

Finally, the long-term cycling performance of Si is shown in Figure 4-14. The specific capacity obtained during the first 1C rate cycle is of 927 mAh/g, which represents only 26% of the theoretical capacity of Si. This result shows that pure Si nanoparticle anodes encounter difficulties in reaching the theoretical capacity values of Si at high cycle rates, presumably due to overpotential losses and the poor electrical conductivity of Si.

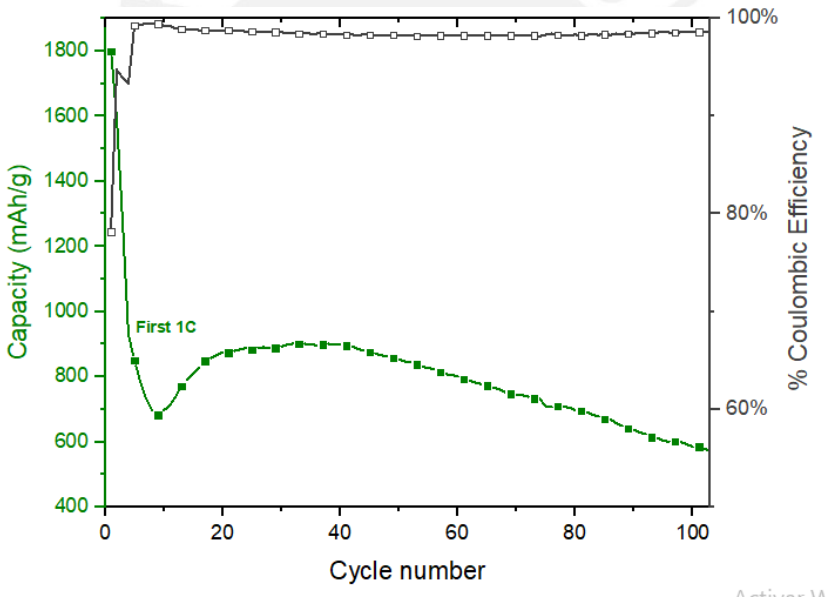

Figure 4-14. Long-term cycling of pure Si anodes at 1C rate current

As the cell is further cycled, a rapid decrease in capacity is observed over the next 5 cycles, reaching a minimum of 700 mAh/g. This capacity is subsequently recovered up to a maximum of 901 mAh/g and maintained until 40 cycles. This effect is not frequently observed in the Si anode literature and the difference could be explained by the cycling procedure, for which a constant current (CC) procedure is usually performed followed by a constant voltage (CV) [100]. Since the experiment performed in this work does not include a CV procedure, it is reasonable to think that

not all Si nanoparticles have been lithiated in the first cycles and, therefore, the activation of these ones increases the capacity in the following cycles. After 40 cycles, most of the Si nanoparticles have been activated and thus a rapid capacity decline is observed in which almost half of the capacity is lost over the next 60 cycles, reaching a capacity of 572 mAh/g at the end of 100 cycles.

In addition, the coulombic efficiency shown in the figure (gray line) increases rapidly during the first 5 cycles up to a maximum of 98.5%, at which it stabilizes. This result shows that, although the main formation of the SEI layer occurs during the first few cycles, it also continues to form throughout the cycles due to the exposure of new Si areas caused by mechanical degradation of the anode. The above is attenuated by the effect of the nanometer size of the Si particles used compared to the results observed for larger particles.

4.3.2 Electrochemical performance of Si-MXene composites

Three Ti_3C_2-Si composite electrodes with Ti_3C_2 composition of 20% (SiMX20), 40% (SiMX40) and 80% (SiMX80) of the active material were cycled under the conditions presented in Section 3.4 and the results of the first three delithiation cycles performed at C/10, C/5 and C/2 are shown in Figure 4-15. In addition, a Si-graphite electrode with 40 wt.% graphite (SiGP40) was also subjected to the same procedure for comparison purposes since graphite is the most common material for preparing Si composite anodes.

As seen in Figure 4-15 and also described previously, the capacity at the slowest C-rate (C/10) of Si is 1798 mAh/g, which is observed to improve to 2011 mAh/g when 20 wt.% Ti_3C_2 is added to the composition. Furthermore, when the content is increased to 40 wt.%, the capacity decreases slightly to 1812 mAh/g, but is still on par with the capacity of the pure Si anode. Finally, when the electrode reaches a Ti_3C_2 content of 80 wt.%, the capacity decreases to 611 mAh/g, the lowest of all the composite electrodes prepared, which is caused by the high Ti_3C_2 content.

Moreover, the experiment in which Ti_3C_2 is replaced by 40 wt.% graphite shows a drastic reduction in capacity to 1427 mAh/g. These results may at first glance seem

contradictory, as the theoretical graphite capacity of 372 mAh/g is almost three times higher than the observed Ti_3C_2 capacity of 110 mAh/g in previous experiments. These results suggest that the addition of Ti_3C_2 promote a better lithiation of Si nanoparticles than graphite and thus enable to achieve a capacity closer to the theoretically expected. In an attempt to support this hypothesis, the theoretical capacity of the different Si-Ti_3C_2 composites were calculated and the results are shown in Figure 4-15. The ratio of experimental capacity related to the theoretical capacity of pure Si is calculated to be 56 %. This is improved to 76%, 89% and 80% for SiMX20, SiMX40 and SiMX80, respectively while the improvement for the SiGP40 is only 69 %.

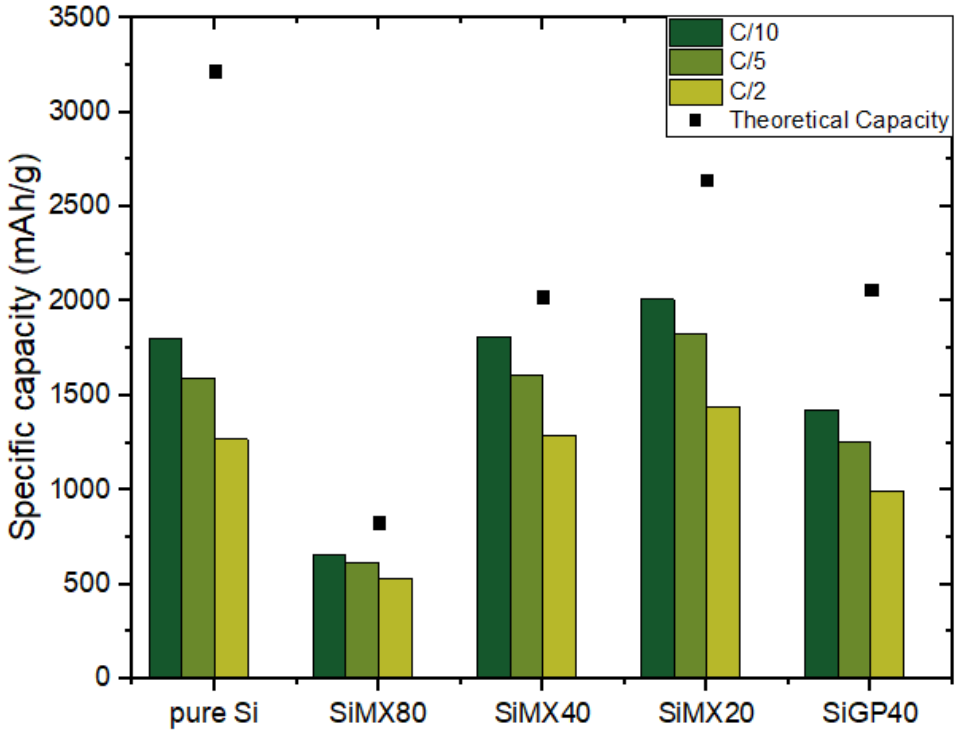

Figure 4-15. Ti_3C_2-Si and Graphite-Si composites theoretical capacity and the three first cycles at C/10, C/5 and C/2 experimental capacities.

Differential capacity analysis was also performed for the three Si-Ti_3C_2 composites and the results are shown in Figure 4-16. The three electrodes show lithiation and delithiation peaks at the same voltage as pure Si. Moreover, the peaks observed for the pure Ti_3C_2 electrode at a C/10 rate are not clearly visible for the SiMX40 (Figure 4-16b) and SiMX20 (Figure 4-16c) electrodes. This could be explained by the high

content and high contribution of Si to the overall capacity of the cell, eclipsing the visibility and interpretation of any Ti_3C_2 peaks. Only in the case of the SiMX80 electrode (Figure 4-16a), a small and broad peak at around 0.45 V, correlated to the Ti_3C_2, is observed during lithiation at C/10. Therefore, it can be concluded that the improvement in Si capacity for the three electrodes does not come from a particular delithiation peak, but from an overall capacity improvement.

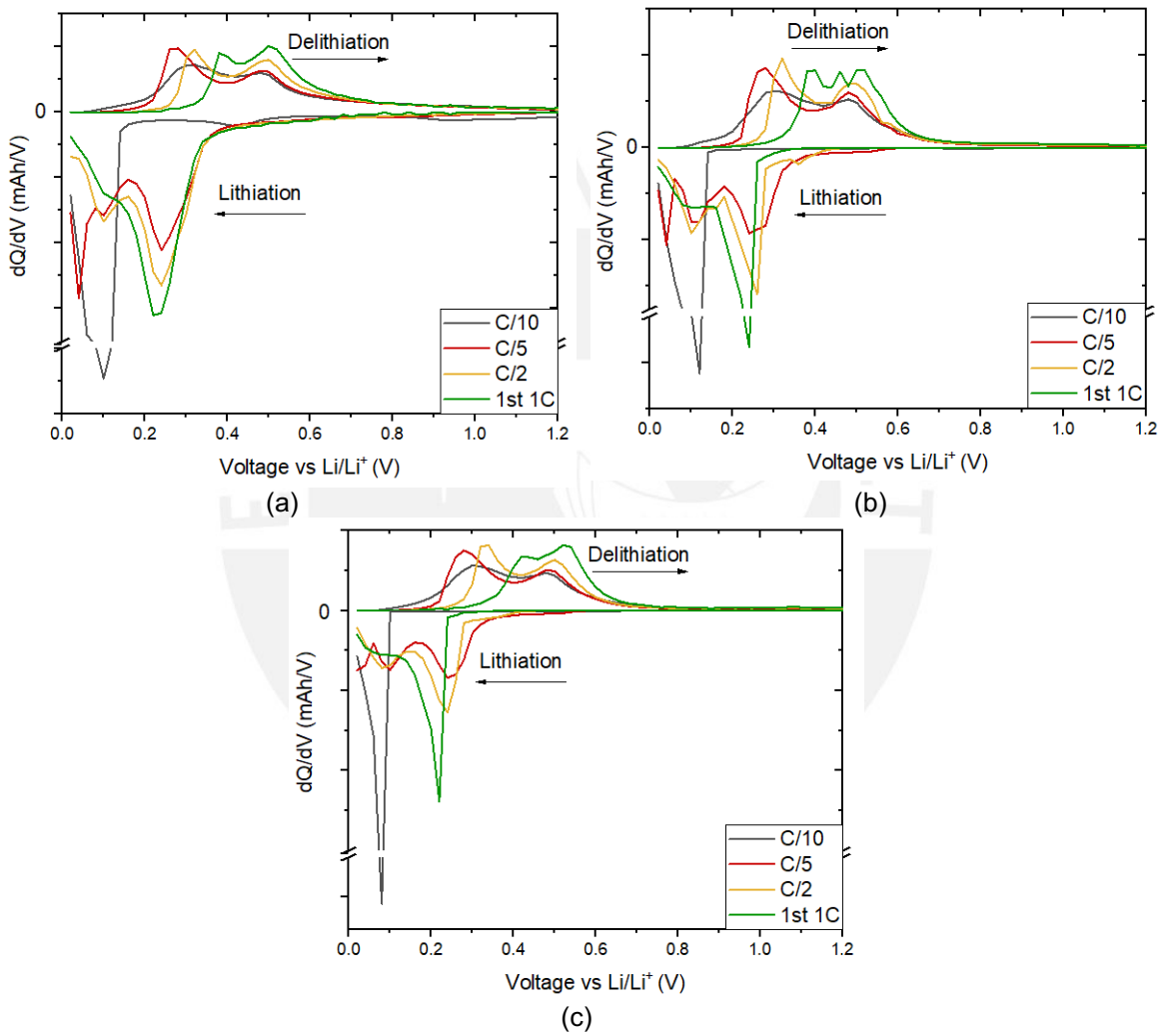

Figure 4-16. Differential capacity analysis of (a) SiMX80 (b) SiMX40 and (c) SiMX20

In addition, potentiostatic electrochemical impedance spectroscopy (PEIS) was performed to characterize the electrochemical processes occurring in the cell and the Nyquist plots for pure Si and Ti_3C_2 - Si composite electrodes are shown in Figure 4-17a. In them, a characteristic behavior of batteries can be observed where a depressed semicircle is observed at medium frequencies followed by a linear slope

at low frequencies. Therefore, the system behavior can be fitted by the equivalent circuit model displayed in in Figure 4-17b where R1 represents the ohmic cell resistance observed at high frequency, R2 represents the charge transfer resistance, Q2 and α_1 represents the double layer capacitance modeled as a constant phase element (CPE) and Q3 and α_2 represents the diffusion effects of Li ions across the electrode. In commercial lithium-ion batteries, a second semicircle, originating from the SEI impedance, is usually present in the Nyquist plot. Since this test was performed before cycling, a second depressed semicircle is not observed and, therefore, no modeling of the SEI layer is necessary.

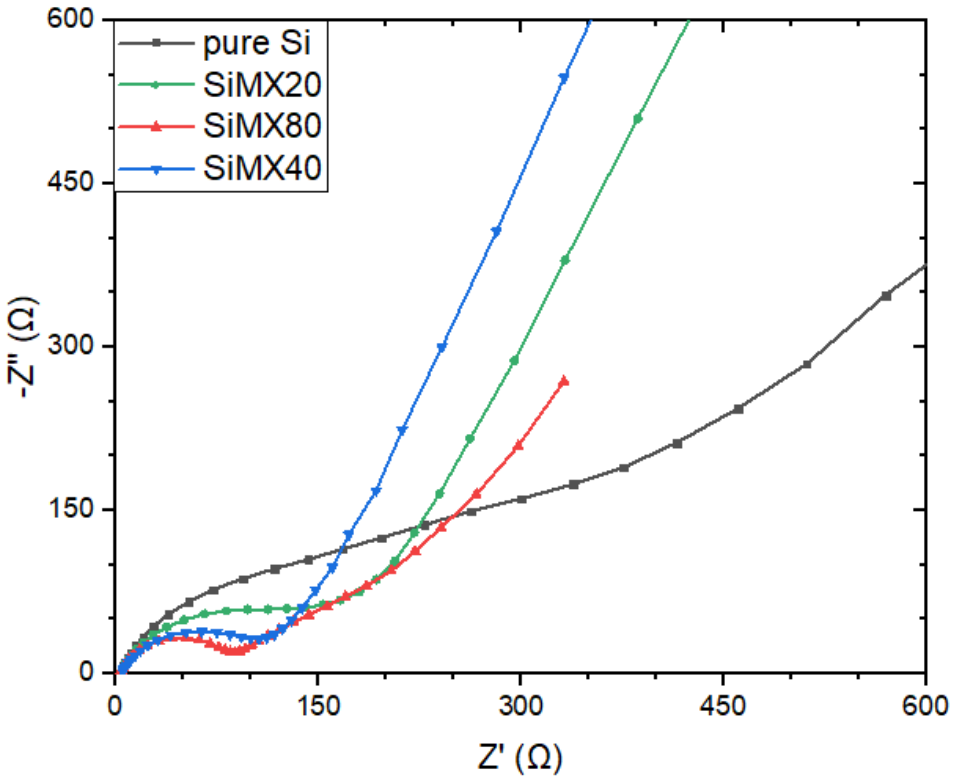

(a)

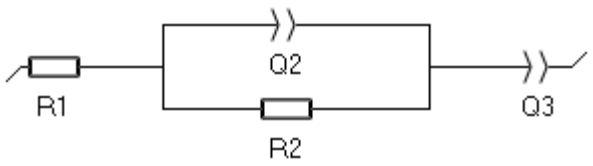

(b)

Figure 4-17. (a) Nyquist plot of pure Si and Ti_3C_2 – Si composite electrodes and (b) equivalent circuit model.

The resulting values of the fitting procedure for all equivalent circuit elements are shown in Table 4-2. The low ohmic resistance observed for pure Si can be explained by the lower loading mass compared to the Ti_3C_2 – Si composites. In the case of the Ti_3C_2 – Si composite, a decrease in the ohmic resistance is observed as Ti_3C_2 content is increased due to its better electrical conductivity. However, the largest reduction is observed in the charge transfer resistance (R2) which is halved in the case of SiMX40 compared to pure Si. Therefore, this reduction explains the reason for the improved Si capacity enabled by Ti_3C_2, as the charge transfer resistance is related to the electrochemical reaction speed and overpotentials occurring during the electrode cycling.

Table 4-2. Values of the equivalent circuit models

Electrode	Model elements					
	R1 (Ω)	Q2 ($\mu F/s^{(1-\alpha 1)}$)	α_1	R2 (Ω)	Q3 ($mF/s^{(1-\alpha 2)}$)	α_2
Si	1.9	7.6	0.82	223	0.3	0.44
SiMX80	2.7	7	0.85	73	3.3	0.51
SiMX40	2.9	14.3	0.75	112	0.54	0.75
SiMX20	3	10	0.75	160	0.25	0.74

Further investigation of the effect of Ti_3C_2 – Si composites in long-term cycling were performed. The results of long-term cycling performed at 1C rates shown in Figure 4-18 evidence that, after 100 cycles, the SiMX20 electrode reached the highest capacity (640 mAh/g), followed by pure Si (572 mAh/g), and closely followed by the SiMX40 electrode (531 mAh/g). Fourth, the silicon-graphite electrode shows only a capacity of 430 mAh/g, which is below the results obtained by the Ti_3C_2 electrode with similar Si content. This suggests that Ti_3C_2 would be a better material for producing silicon composite anodes. Moreover, the SiMX80 electrode shows a capacity of 257 mAh/g due to the low Si content. This result is still better than the pure graphite electrode (116 mAh/g at 1C rate) build for reference purpose.

The advantages of electrodes containing Ti_3C_2 over long-term cycling are clearer when considering the amount of mass loading achieved during the current collector coating. For this purpose, the areal capacity was calculated by dividing the absolute

capacity obtained at the end of the 100 cycles by the area of the 11 mm circular current collector and the results are shown in Figure 4-18b. According to this metric, the SiMX40 electrode obtained the highest results, followed closely by SiMX20 and SiGP40. The pure Si anode performed worse according to this metric due to the low mass loading obtained during electrode preparation. This metric is of vital importance for the LIB industry as it aims to increase the amount of active material in a cell relative to the mass/volume occupied by the current collector. Therefore, it can be concluded that Ti_3C_2 - Si composite electrodes with higher capacity than pure Si anodes can be produced.

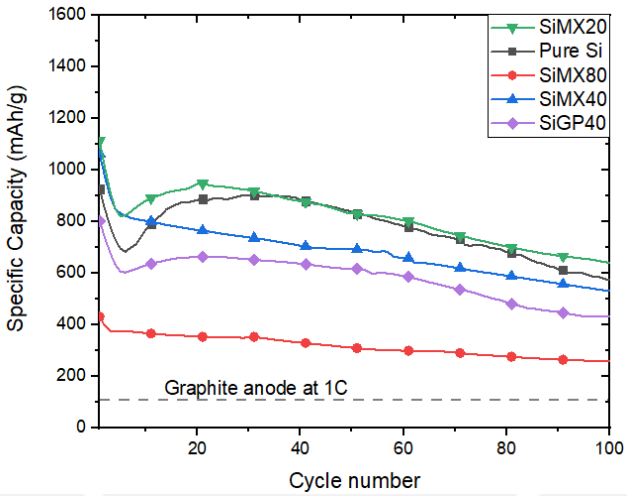

(a)

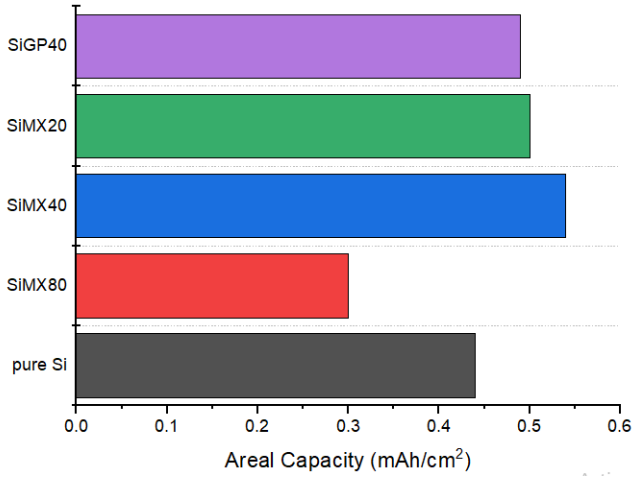

(b)

Figure 4- 18. (a) Long-term cycling specific capacity of electrodes at 1C rate and (b) Areal capacity at the last 1C 100th cycle.

Following the same method used previously for pure Si anodes, the hysteresis evolution of 1C rate cycles was calculated for Si composite anodes and the results are shown in Figure 4-20. A clear reduction in hysteresis is observed during the first cycle for all Si composites compared to pure Si anodes, with an improvement as the Ti_3C_2 content increases. As the results correspond to the same cycle rate, it is reasonable to think that the increase in hysteresis is due to a higher internal resistance originated by the mechanical degradation of the electrode. Therefore, it can be presumed that the increase in hysteresis is directly related to the periodic volume change of the electrode and the mechanical stress it undergoes during cycling. Under this presumption, it can be proposed that graphite reliefs Si expansion better than Ti_3C_2, although further examination is required to accept this hypothesis.

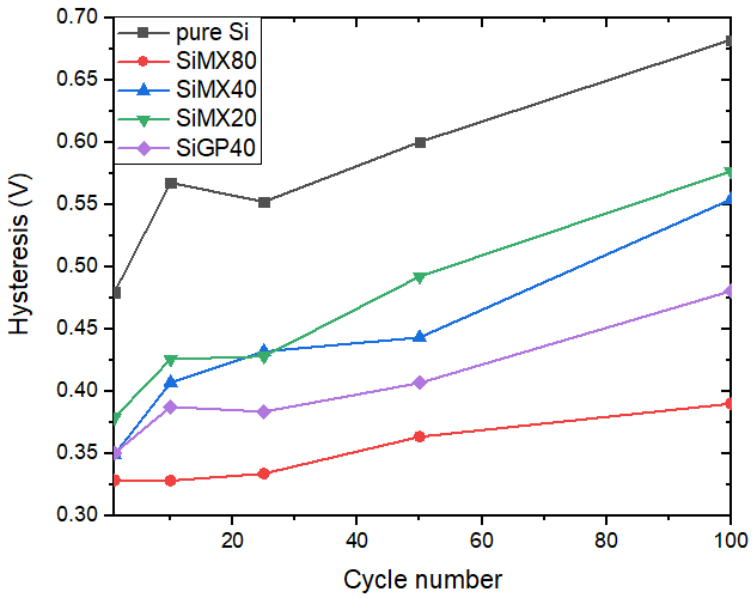

Figure 4- 19. Hysteresis evolution of Si and Si composite anodes

5. Conclusions and outlook

Silicon is one of the candidates to replace graphite in commercial lithium-ion batteries due to its high theoretical capacity. However, the high mechanical stress suffered by Si electrodes caused by volumetric expansion and its low electrical conductivity remain challenges to be addressed. In order to study the possibility to overcome those challenges, this work has focused on the synthesis of Ti_3C_2 - Si composites as anode materials as well as to study their electrochemical performance. Ti_3C_2 is a two-dimensional material whose good mechanical strength and electrical conductivity can contribute to solving the problems of Si anodes.

The investigation of the active materials used in this thesis revealed, that silicon nanopowder used in the present work exhibits a particle size in the nanoscale range with a round shape in agreement with the supplier statements (Section 4.1.1). Multilayered Ti_3C_2 particles exhibits a particle size in the microscale and exhibit an accordion-like structure. A high fluorine content was observed by EDS and can be ascribed to its previous synthesis via selective chemical etching process with concentrated HF solution. (Section 4.1.2).

A reproducible electrode preparation technique for slurries of low volume (<5 mL) was developed for Si, Ti_3C_2, graphite and composites. It has been found that the synthesis of composite electrodes not only improves the processability of the pure Si slurry and electrode density but also reduces the occurrence of cracks over the surface as the Si content decreases (Section 4.2). SEM investigations of the as-prepared Ti_3C_2 – Si composites electrodes show that the interaction between Si nanoparticles and Ti_3C_2 seems to be mainly superficial, no clear evidence of the presence of Si particles inside of the accordion structures of the MXene was observed.

The study of the electrochemical performance of Ti_3C_2 – Si composites were performed in half-cells with lithium as counterelectrode. It was shown that the addition of Ti_3C_2 to Si anodes enables Si to reach its theoretical potential, a task in which it surpasses graphite – Si composites (Section 4.3.2). The explanation resides in the reduction of the charge transfer resistance of the electrodes containing Ti_3C_2.

In the long-term cycling experiment, SiMX20 and SiMX40 exhibit the highest specific and areal capacities after 100 cycles, respectively. However, the capacity retention does not seem clearly improved by the addition of Ti_3C_2. More investigation in this regard is required to confirm this hypothesis. Furthermore, addition of Ti_3C_2 reduces the voltage hysteresis observed in Si anodes for long-term cycling experiments and, therefore, higher energy efficiencies during charging/discharging cycles can be achieved by Ti_3C_2 – Si composites.

Future work should focus on the improvement of the preparation of the Ti_3C_2 – silicon composite anodes as this clearly has a direct effect on the composite electrode performance, particularly in long-term cycling experiments. Furthermore, the delamination of Ti_3C_2 multilayers is suggested under the procedures provided in the literature review [64]. The use of monolayered Ti_3C_2 might show higher capacities than their multilayer form and its use could facilitate the intercalation of Si nanoparticles between layers. The study of the mechanical stress and expansion is of vital importance for Si anodes and, therefore, it is also interesting the use of other characterization techniques such as dilatometry and force sensor cycling tests to confirm the stress relief effect provided by Ti_3C_2 in silicon composites. Finally, the use of Ti_3C_2 with different functional groups and MXenes of different transition metals and composition are suggested. Particularly MXenes of the chemical formula M_2X such as Ti_2C and V_2C are of special interest due to their lower mass per layer.

6. References

[1] W. F. Lamb *et al.*, “A review of trends and drivers of greenhouse gas emissions by sector from 1990 to 2018,” *Environ. Res. Lett.*, vol. 16, no. 7, p. 073005, Jun. 2021.

[2] G. Zubi, R. Dufo-López, M. Carvalho, and G. Pasaoglu, “The lithium-ion battery: State of the art and future perspectives,” *Renew. Sustain. Energy Rev.*, vol. 89, no. April 2017, pp. 292–308, 2018.

[3] A. Manthiram, “A reflection on lithium-ion battery cathode chemistry,” *Nat. Commun.*, vol. 11, no. 1, pp. 1–9, 2020.

[4] Jakob Asenbauer, Tobias Eisenmann, Matthias Kuenzel, Arefeh Kazzazi, Zhen Chen, and Dominic Bresser, “The success story of graphite as a lithium-ion anode material – fundamentals, remaining challenges, and recent developments including silicon (oxide) composites,” *Sustain. Energy Fuels*, vol. 4, no. 11, pp. 5387–5416, Oct. 2020.

[5] X. Zuo, J. Zhu, P. Müller-Buschbaum, and Y. J. Cheng, “Silicon based lithium-ion battery anodes: A chronicle perspective review,” *Nano Energy*, vol. 31, pp. 113–143, Jan. 2017.

[6] Y. Jin, B. Zhu, Z. Lu, N. Liu, and J. Zhu, “Challenges and Recent Progress in the Development of Si Anodes for Lithium-Ion Battery,” *Adv. Energy Mater.*, vol. 7, no. 23, p. 1700715, Dec. 2017.

[7] S. Chae, S.-H. Choi, N. Kim, J. Sung, and J. Cho, “Integration of Graphite and Silicon Anodes for the Commercialization of High-Energy Lithium-Ion Batteries,” *Angew. Chemie Int. Ed.*, vol. 59, no. 1, pp. 110–135, Jan. 2020.

[8] C. (John) Zhang *et al.*, “High capacity silicon anodes enabled by MXene viscous aqueous ink,” *Nat. Commun. 2019 101*, vol. 10, no. 1, pp. 1–9, Feb. 2019.

[9] X. Tang, X. Guo, W. Wu, and G. Wang, “2D Metal Carbides and Nitrides (MXenes) as High-Performance Electrode Materials for Lithium-Based Batteries,” *Adv. Energy Mater.*, vol. 8, no. 33, p. 1801897, Nov. 2018.

[10] A. VahidMohammadi, J. Rosen, and Y. Gogotsi, “The world of two-dimensional carbides and nitrides (MXenes),” *Science (80-.).*, vol. 372, no. 6547, Jun. 2021.

[11] S. Jiao *et al.*, “Behavior of Lithium Metal Anodes under Various Capacity Utilization and High Current Density in Lithium Metal Batteries,” *Joule*, vol. 2, no. 1, pp. 110–124, 2018.

[12] M. S. Whittingham, “History, evolution, and future status of energy storage,” *Proc. IEEE*, vol. 100, no. SPL CONTENT, pp. 1518–1534, May 2012.

[13] Birger Horstmann *et al.*, “Strategies towards enabling lithium metal in

batteries: interphases and electrodes," *Energy Environ. Sci.*, 2021.

[14] J. Asenbauer, T. Eisenmann, M. Kuenzel, A. Kazzazi, Z. Chen, and D. Bresser, "The success story of graphite as a lithium-ion anode material – fundamentals, remaining challenges, and recent developments including silicon (oxide) composites," *Sustain. Energy Fuels*, 2020.

[15] K. Mizushima, P. C. Jones, P. J. Wiseman, and J. B. Goodenough, "LixCoO2 (0<x<-1): A new cathode material for batteries of high energy density," *Mater. Res. Bull.*, vol. 15, no. 6, pp. 783–789, Jun. 1980.

[16] M. Winter, B. Barnett, and K. Xu, "Before Li Ion Batteries," *Chem. Rev.*, vol. 118, no. 23, pp. 11433–11456, Dec. 2018.

[17] Y. Nishi, "Lithium ion secondary batteries; past 10 years and the future."

[18] R. Korthauer, *Lithium-ion batteries: Basics and applications*. 2018.

[19] S. J. An, J. Li, C. Daniel, D. Mohanty, S. Nagpure, and D. L. Wood, "The state of understanding of the lithium-ion-battery graphite solid electrolyte interphase (SEI) and its relationship to formation cycling," *Carbon N. Y.*, vol. 105, pp. 52–76, Aug. 2016.

[20] W. J. Zhang, "A review of the electrochemical performance of alloy anodes for lithium-ion batteries," *Journal of Power Sources*, vol. 196, no. 1. pp. 13–24, 01-Jan-2011.

[21] K. Wang *et al.*, "Recent advances and historical developments of high voltage lithium cobalt oxide materials for rechargeable Li-ion batteries," *J. Power Sources*, vol. 460, p. 228062, Jun. 2020.

[22] N. Nitta, F. Wu, J. T. Lee, and G. Yushin, "Li-ion battery materials: Present and future," *Mater. Today*, vol. 18, no. 5, pp. 252–264, 2015.

[23] Y. Huang *et al.*, "Lithium Manganese Spinel Cathodes for Lithium-Ion Batteries," *Adv. Energy Mater.*, vol. 11, no. 2, p. 2000997, Jan. 2021.

[24] W. J. Zhang, "Structure and performance of LiFePO4 cathode materials: A review," *J. Power Sources*, vol. 196, no. 6, pp. 2962–2970, 2011.

[25] M. Stich, *Wasserverunreinigungen in Lithium-Ionen-Batterien*. Ilmenau, 2019.

[26] G.-C. Chung, H.-J. Kim, S.-I. Yu, S.-H. Jun, J. Choi, and M.-H. Kim, "Origin of Graphite Exfoliation - An Investigation of the Important Role of Solvent Cointercalation," 2000.

[27] B. M. Winter, J. O. Besenhard, M. E. Spahr, and P. Novμk, "Insertion Electrode Materials for Rechargeable Lithium Batteries **," no. 10, pp. 725–763, 1998.

[28] C. P. Sandhya, B. John, and C. Gouri, "Lithium titanate as anode material for lithium-ion cells : a review," pp. 601–620, 2014.

[29] W. J. Zhang, "A review of the electrochemical performance of alloy anodes for

lithium-ion batteries," *J. Power Sources*, vol. 196, no. 1, pp. 13–24, Jan. 2011.

[30] H. F. Andersen *et al.*, "Silicon-Carbon composite anodes from industrial battery grade silicon," *Sci. Reports 2019 91*, vol. 9, no. 1, pp. 1–9, Oct. 2019.

[31] E. Quartarone and P. Mustarelli, "Review—Emerging Trends in the Design of Electrolytes for Lithium and Post-Lithium Batteries," *J. Electrochem. Soc.*, vol. 167, no. 5, p. 050508, 2020.

[32] M. Stich, M. Göttlinger, M. Kurniawan, U. Schmidt, and A. Bund, "Hydrolysis of LiPF6 in Carbonate-Based Electrolytes for Lithium-Ion Batteries and in Aqueous Media," *J. Phys. Chem. C*, vol. 122, no. 16, pp. 8836–8842, 2018.

[33] M. Marcinek *et al.*, "Electrolytes for Li-ion transport - Review," *Solid State Ionics*, vol. 276, pp. 107–126, 2015.

[34] S. S. Zhang, "A review on electrolyte additives for lithium-ion batteries," *J. Power Sources*, vol. 162, no. 2 SPEC. ISS., pp. 1379–1394, 2006.

[35] H. Lee, M. Yanilmaz, O. Toprakci, K. Fu, and X. Zhang, "A review of recent developments in membrane separators for rechargeable lithium-ion batteries," *Energy Environ. Sci.*, vol. 7, no. 12, pp. 3857–3886, Nov. 2014.

[36] P. Zhu, D. Gastol, J. Marshall, R. Sommerville, V. Goodship, and E. Kendrick, "A review of current collectors for lithium-ion batteries," *J. Power Sources*, vol. 485, p. 229321, Feb. 2021.

[37] M. N. Obrovac and L. Christensen, "Structural changes in silicon anodes during lithium insertion/extraction," *Electrochem. Solid-State Lett.*, vol. 7, no. 5, pp. 93–96, 2004.

[38] A. G. Morachevskii and A. I. Demidov, "Lithium-silicon alloys: Phase diagram, electrochemical studies, thermodynamic properties, application in chemical power cells," *Russ. J. Appl. Chem.*, vol. 88, no. 4, pp. 547–566, 2015.

[39] M. Zeilinger, I. M. Kurylyshyn, U. Häussermann, and T. F. Fässler, "Revision of the li-si phase diagram: Discovery and single-crystal x-ray structure determination of the high-temperature phase li4.11si," *Chem. Mater.*, vol. 25, no. 22, pp. 4623–4632, 2013.

[40] M. N. Obrovac and L. J. Krause, "Reversible Cycling of Crystalline Silicon Powder," *J. Electrochem. Soc.*, vol. 154, no. 2, p. A103, 2007.

[41] X. Zuo, J. Zhu, P. Müller-Buschbaum, and Y. J. Cheng, "Silicon based lithium-ion battery anodes: A chronicle perspective review," *Nano Energy*, vol. 31, no. November 2016, pp. 113–143, 2017.

[42] U. Kasavajjula, C. Wang, and A. J. Appleby, "Nano- and bulk-silicon-based insertion anodes for lithium-ion secondary cells," *J. Power Sources*, vol. 163, no. 2, pp. 1003–1039, 2007.

[43] X. H. Liu, L. Zhong, S. Huang, S. X. Mao, T. Zhu, and J. Y. Huang, "Size-Dependent Fracture of Silicon Nanoparticles During Lithiation," *ACS Nano*,

vol. 6, no. 2, pp. 1522–1531, Feb. 2012.

[44] Y. Jin, B. Zhu, Z. Lu, N. Liu, and J. Zhu, “Challenges and Recent Progress in the Development of Si Anodes for Lithium-Ion Battery,” *Adv. Energy Mater.*, vol. 7, no. 23, p. 1700715, Dec. 2017.

[45] X. Zhao and V.-P. Lehto, “Challenges and prospects of nanosized silicon anodes in lithium-ion batteries,” *Nanotechnology*, vol. 32, no. 4, p. 042002, Oct. 2020.

[46] C. Zhang *et al.*, “Challenges and Recent Progress on Silicon-Based Anode Materials for Next-Generation Lithium-Ion Batteries,” *Small Struct.*, vol. 2, no. 6, p. 2100009, Jun. 2021.

[47] M. Ge, X. Fang, J. Rong, and C. Zhou, “Review of porous silicon preparation and its application for lithium-ion battery anodes,” *Nanotechnology*, vol. 24, pp. 422001–422011, 2013.

[48] H. Kim, E.-J. Lee, and Y.-K. Sun, “Recent advances in the Si-based nanocomposite materials as high capacity anode materials for lithium ion batteries,” *Biochem. Pharmacol.*, vol. 00, 2014.

[49] “Study of the Binder Influence on Expansion/Contraction Behavior of Silicon Alloy Negative Electrodes for Lithium-Ion Batteries,” 2020.

[50] O. Naboka, C.-H. Yim, and Y. Abu-Lebdeh, “Practical Approach to Enhance Compatibility in Silicon/Graphite Composites to Enable High-Capacity Li-Ion Battery Anodes,” *ACS Omega*, vol. 6, no. 4, pp. 2644–2654, Feb. 2021.

[51] W. M. Dose, M. J. Piernas-Muñoz, V. A. Maroni, S. E. Trask, I. Bloom, and C. S. Johnson, “Capacity fade in high energy silicon-graphite electrodes for lithium-ion batteries,” *Chem. Commun.*, vol. 54, no. 29, pp. 3586–3589, Apr. 2018.

[52] J. Moon *et al.*, “Interplay between electrochemical reactions and mechanical responses in silicon–graphite anodes and its impact on degradation,” *Nat. Commun.*, vol. 12, no. 1, 2021.

[53] G. G. Eshetu *et al.*, “Production of high-energy Li-ion batteries comprising silicon-containing anodes and insertion-type cathodes,” *Nat. Commun. 2021 121*, vol. 12, no. 1, pp. 1–14, Sep. 2021.

[54] P. Li, H. Kim, S. T. Myung, and Y. K. Sun, “Diverting Exploration of Silicon Anode into Practical Way: A Review Focused on Silicon-Graphite Composite for Lithium Ion Batteries,” *Energy Storage Mater.*, vol. 35, pp. 550–576, 2021.

[55] J. B. Park, J. S. Ham, M. S. Shin, H. K. Park, Y. J. Lee, and S. M. Lee, “Synthesis and electrochemical characterization of anode material with titanium–silicon alloy solid core/nanoporous silicon shell structures for lithium rechargeable batteries,” *J. Power Sources*, vol. 299, pp. 537–543, Dec. 2015.

[56] S. Chae, S.-H. Choi, N. Kim, J. Sung, and J. Cho, “Integration of Graphite and Silicon Anodes for the Commercialization of High-Energy Lithium-Ion Batteries,” *Angew. Chemie Int. Ed.*, vol. 59, no. 1, pp. 110–135, Jan. 2020.

[57] N. Kim, S. Chae, J. Ma, M. Ko, and J. Cho, “Fast-charging high-energy lithium-ion batteries via implantation of amorphous silicon nanolayer in edge-plane activated graphite anodes,” *Nat. Commun. 2017 81*, vol. 8, no. 1, pp. 1–10, Oct. 2017.

[58] B. Anasori, M. R. Lukatskaya, and Y. Gogotsi, *2D metal carbides and nitrides (MXenes) for energy storage*, vol. 2, no. 2. 2017.

[59] M. Sokol, V. Natu, S. Kota, and M. W. Barsoum, “On the Chemical Diversity of the MAX Phases,” *Trends Chem.*, vol. 1, no. 2, pp. 210–223, May 2019.

[60] M. Naguib *et al.*, “Two-dimensional nanocrystals produced by exfoliation of Ti 3AlC 2,” *Adv. Mater.*, vol. 23, no. 37, pp. 4248–4253, Oct. 2011.

[61] O. Salim, K. A. Mahmoud, K. K. Pant, and R. K. Joshi, “Introduction to MXenes: synthesis and characteristics,” *Mater. Today Chem.*, vol. 14, p. 100191, 2019.

[62] O. Mashtalir *et al.*, “Intercalation and delamination of layered carbides and carbonitrides,” *Nat. Commun. 2013 41*, vol. 4, no. 1, pp. 1–7, Apr. 2013.

[63] M. Ghidiu, M. R. Lukatskaya, M. Q. Zhao, Y. Gogotsi, and M. W. Barsoum, “Conductive two-dimensional titanium carbide ‘clay’ with high volumetric capacitance,” *Nature*, vol. 516, no. 7529, pp. 78–81, 2015.

[64] M. Alhabeb *et al.*, “Guidelines for Synthesis and Processing of Two-Dimensional Titanium Carbide (Ti3C2Tx MXene),” *Chem. Mater.*, vol. 29, no. 18, pp. 7633–7644, Sep. 2017.

[65] F. Liu *et al.*, “Preparation of Ti 3 C 2 and Ti 2 C MXenes by fluoride salts etching and methane adsorptive properties,” *Appl. Surf. Sci.*, vol. 416, pp. 781–789, 2017.

[66] T. Li *et al.*, “Fluorine-Free Synthesis of High-Purity Ti3C2Tx (T=OH, O) via Alkali Treatment,” *Angew. Chemie - Int. Ed.*, vol. 57, no. 21, pp. 6115–6119, 2018.

[67] S. Yang *et al.*, “Fluoride-Free Synthesis of Two-Dimensional Titanium Carbide (MXene) Using A Binary Aqueous System,” *Angew. Chemie - Int. Ed.*, vol. 57, no. 47, pp. 15491–15495, 2018.

[68] X. H. Zha *et al.*, “Role of the surface effect on the structural, electronic and mechanical properties of the carbide MXenes,” *Epl*, vol. 111, no. 2, 2015.

[69] Z. Li *et al.*, “Synthesis and thermal stability of two-dimensional carbide MXene Ti3C2,” *Mater. Sci. Eng. B Solid-State Mater. Adv. Technol.*, vol. 191, no. C, pp. 33–40, Jan. 2015.

[70] T. Habib *et al.*, “Oxidation stability of Ti3C2Tx MXene nanosheets in solvents and composite films,” *npj 2D Mater. Appl.*, vol. 3, no. 1, pp. 1–6, Dec. 2019.

[71] D. Er, J. Li, M. Naguib, Y. Gogotsi, and V. B. Shenoy, “Ti 3 C 2 MXene as a High Capacity Electrode Material for Metal (Li, Na, K, Ca) Ion Batteries,” 2014.

[72] Q. Tang, Z. Zhou, and P. Shen, “Are MXenes Promising Anode Materials for Li Ion Batteries? Computational Studies on Electronic Properties and Li Storage Capability of Ti3C2 and Ti3C2X2 (X = F, OH) Monolayer,” *J. Am. Chem. Soc.*, vol. 134, no. 40, pp. 16909–16916, Oct. 2012.

[73] D. Sun, M. Wang, Z. Li, G. Fan, L.-Z. Fan, and A. Zhou, “Two-dimensional Ti 3 C 2 as anode material for Li-ion batteries,” 2014.

[74] F. Kong *et al.*, “Improving the electrochemical properties of MXene Ti 3 C 2 multilayer for Li-ion batteries by vacuum calcination,” *Electrochim. Acta*, 2018.

[75] Y. Xie *et al.*, “Role of Surface Structure on Li-Ion Energy Storage Capacity of Two-Dimensional Transition-Metal Carbides,” *J. Am. Chem. Soc.*, vol. 136, no. 17, pp. 6385–6394, Apr. 2014.

[76] Z. Lin, H. Shao, K. Xu, P.-L. Taberna, and P. Simon, “MXenes as High-Rate Electrodes for Energy Storage,” *Trends Chem.*, vol. 2020, no. 7.

[77] J.-C. Lei, X. Zhang, and Z. Zhou, “Recent advances in MXene: Preparation, properties, and applications,” *Front. Phys*, vol. 10, p. 107303, 2015.

[78] A. J. D. Nanomaterials, B. Anasori, M. R. Lukatskaya, and Y. Gogotsi, “2D metal carbides and nitrides (MXenes) for energy storage,” 2017.

[79] Y. Zhu, K. Rajouâ, S. Le Vot, O. Fontaine, P. Simon, and F. Favier, “Modifications of MXene layers for supercapacitors,” *Nano Energy*, vol. 73, p. 104734, Jul. 2020.

[80] B. Ahmed, D. H. Anjum, M. N. Hedhili, Y. Gogotsi, and H. N. Alshareef, “H2O2 assisted room temperature oxidation of Ti2C MXene for Li-ion battery anodes,” *Nanoscale*, vol. 8, no. 14, pp. 7580–7587, Mar. 2016.

[81] Y.-T. Du, X. Kan, F. Yang, L.-Y. Gan, and U. Schwingenschlögl, “MXene/Graphene Heterostructures as High-Performance Electrodes for Li-Ion Batteries,” *ACS Appl. Mater. Interfaces*, vol. 10, no. 38, pp. 32867–32873, Sep. 2018.

[82] C. Chen *et al.*, “MoS2-on-MXene Heterostructures as Highly Reversible Anode Materials for Lithium-Ion Batteries,” *Angew. Chemie*, vol. 130, no. 7, pp. 1864–1868, Feb. 2018.

[83] D. chuan Zuo, S. chao Song, C. sheng An, L. bo Tang, Z. jiang He, and J. chao Zheng, “Synthesis of sandwich-like structured Sn/SnOx@MXene composite through in-situ growth for highly reversible lithium storage,” *Nano Energy*, vol. 62, pp. 401–409, Aug. 2019.

[84] F. Kong *et al.*, “Enhanced reversible Li-ion storage in Si@Ti3C2 MXene nanocomposite,” *Electrochem. commun.*, vol. 97, pp. 16–21, Dec. 2018.

[85] X. Zhu *et al.*, “Enhanced cycling performance of Si-MXene nanohybrids as

anode for high performance lithium ion batteries," *Chem. Eng. J.*, vol. 378, p. 122212, Dec. 2019.

[86] H. Li *et al.*, "Employing MXene as a matrix for loading amorphous Si generated upon lithiation towards enhanced lithium-ion storage," *J. Energy Chem.*, vol. 38, pp. 50–54, Nov. 2019.

[87] X. Hui, R. Zhao, P. Zhang, C. Li, C. Wang, and L. Yin, "Low-Temperature Reduction Strategy Synthesized Si/Ti3C2 MXene Composite Anodes for High-Performance Li-Ion Batteries," *Adv. Energy Mater.*, vol. 9, no. 33, p. 1901065, Sep. 2019.

[88] M. Xia *et al.*, "Ti3C2Tx MXene Nanosheets as a Robust and Conductive Tight on Si Anodes Significantly Enhance Electrochemical Lithium Storage Performance," *ACS Nano*, vol. 14, no. 4, pp. 5111–5120, Apr. 2020.

[89] F. Zhang *et al.*, "Sandwich-like silicon/Ti3C2Tx MXene composite by electrostatic self-assembly for high performance lithium ion battery," *Energy*, vol. 195, p. 117047, Mar. 2020.

[90] C. (John) Zhang *et al.*, "High capacity silicon anodes enabled by MXene viscous aqueous ink," *Nat. Commun. 2019 101*, vol. 10, no. 1, pp. 1–9, Feb. 2019.

[91] K. T. Sarang *et al.*, "Minimizing two-dimensional Ti3C2Tx MXene nanosheet loading in carbon-free silicon anodes," *Nanoscale*, vol. 12, no. 40, pp. 20699–20709, Oct. 2020.

[92] Y. Tian, Y. An, and J. Feng, "Flexible and Freestanding Silicon/MXene Composite Papers for High-Performance Lithium-Ion Batteries," *ACS Appl. Mater. Interfaces*, vol. 11, no. 10, pp. 10004–10011, Mar. 2019.

[93] M. Marian *et al.*, "Mxene nanosheets as an emerging solid lubricant for machine elements – Towards increased energy efficiency and service life," *Appl. Surf. Sci.*, vol. 523, p. 146503, Sep. 2020.

[94] V. Murray, D. S. Hall, and J. R. Dahn, "A Guide to Full Coin Cell Making for Academic Researchers," *J. Electrochem. Soc.*, vol. 166, no. 2, p. A329, Jan. 2019.

[95] H. Wiggers, R. Starke, and P. Roth, "Silicon Particle Formation by Pyrolysis of Silane in a Hot Wall Gasphase Reactor."

[96] M. Hu *et al.*, "Surface Functional Groups and Interlayer Water Determine the Electrochemical Capacitance of Ti3C2Tx MXene," *ACS Nano*, vol. 12, no. 4, pp. 3578–3586, Apr. 2018.

[97] K. Rollag, D. Juarez-Robles, Z. Du, D. L. Wood, and P. P. Mukherjee, "Drying Temperature and Capillarity-Driven Crack Formation in Aqueous Processing of Li-Ion Battery Electrodes," 2019.

[98] D. Sun, M. Wang, Z. Li, G. Fan, L. Z. Fan, and A. Zhou, "Two-dimensional

Ti3C2 as anode material for Li-ion batteries," *Electrochem. commun.*, vol. 47, pp. 80–83, Oct. 2014.

[99] C. Jin, H. Li, Y. Song, B. Lu, A. K. Soh, and J. Zhang, "On stress-induced voltage hysteresis in lithium ion batteries: Impacts of surface effects and interparticle compression," *Sci. China Technol. Sci. 2019 628*, vol. 62, no. 8, pp. 1357–1364, Jun. 2019.

[100] M. Holzapfel *et al.*, "Nano silicon for lithium-ion batteries," *Electrochim. Acta*, vol. 52, pp. 973–978, 2006.